

AD-A238 848



2

Technical Report 1411
February 1991

Long-Distance Repeaterless Duplex Fiber-Optic Demonstration System

M. R. Brininstool
S. J. Cowen
W. H. Marn
M. C. Scallion

DTIC
ELECTE
JUL 29 1991
S B D

DEFENSE TECHNICAL INFORMATION CENTER



9106287

Approved for public release; distribution is unlimited.

91 7 29 011

NAVAL OCEAN SYSTEMS CENTER

San Diego, California 92152-5000

J. D. FONTANA, CAPT, USN
Commander

H. R. TALKINGTON, Acting
Technical Director

ADMINISTRATIVE INFORMATION

The work reported here was performed by the Advanced Concepts Branch, Code 946, Naval Ocean Systems Center, for the Chief of Naval Operations, OP-924, Office of Naval Research, Code 01123, under program element 3000N, project number CG92.

Released by
S. J. Cowen, Head
Advanced Concepts Branch

Under authority of
N. B. Estabrook, Head
Ocean Engineering
Division

ACKNOWLEDGMENTS

The authors gratefully acknowledge the assistance of Jim Daughtry, Susan Hampton, and Joe Morales in providing ongoing technical support to the demonstration project.

SUMMARY

OVERVIEW

This report updates Naval Ocean Systems Center Technical Report 1185, "104-km Unrepeated Bidirectional Fiber-optic Demonstration Link," (Brininstool, 1987). Provided are discussions on improvements made to the original demonstration system. These include enhanced receiver sensitivities, increased laser-transmitter optical power outputs, refined operation of the PFM and Manchester encoding subsystems, and reduced splice losses. Also discussed is the emerging technology of fiber amplifiers that promise to significantly extend the repeaterless distance beyond the present range.

RESULTS

Several system improvements have resulted in increased standoff range compared to the previous 104-km demonstration. The present standoff range is 153 km. This includes a 5-dB safety factor. An optimum standoff of 186 km was calculated based on a minimum value for fiber attenuation at 1300 of 0.384 dB/km. Most of the gain in standoff range was achieved by increasing the laser transmitter output powers and increasing the receiver sensitivities for both 1300- and 1550-nm channels. Margin improvements of 17.6 and 6.5 dB were attained for the 1300- and 1550-nm channels respectively. The higher laser powers were obtained by simply replacing the previous lasers with more technically mature transmitters. Gains of 6.6 dB at 1300 nm and 0.5 dB at 1550 nm were achieved in this way. The 1300-nm PIN-FET receiver is replaced with a low-noise PIN photodiode/integrating front-end receiver. A gain of 11 dB is noted. The 1550-nm receiver is replaced with an Avalanche Photodiode (APD) receiver, yielding 4-dB improved sensitivity. The pulse frequency modulation (PFM) circuitry was changed to transmit longer pulse widths, thereby requiring a smaller receiver bandwidth. This change in bandwidth gave an additional 2-dB gain. An erbium-doped fiber amplifier (EDFA) was purchased and will be installed into the system in FY 91. Gains to the 1550-nm receiver sensitivity of 10 dB or more are expected. Details on these changes and future plans for the system are given in the body of the report. The improvements detailed in this report are summarized in table 1.

Table 1. Summary of system improvements.

Channel	Improvement	Gain in margin (dB)
1300 nm	Higher power laser	6.6
	Ultrasensitive receiver	11.0
	Total	17.6 dB
1550 nm	New laser	0.5
	APD receiver	4.0
	Reduced receiver bandwidth	2.0
	Total	6.5 dB

Accession For

NTIS GRA&I ☒

DTIC TAB ☐

Unannounced ☐

Justification

By

Distribution/

Availability Codes

Dist	Avail and/or Special
A-1	



CONTENTS

1.0 SYSTEM-LEVEL CONSIDERATIONS	1
1.1 Impacts of Laser Parameters on Standoff Range	1
1.1.1 Loss-Limited Standoff Range	1
1.1.2 Bandwidth-Limited Standoff Range	2
2.0 OPTICAL POWER BUDGETS	4
2.1 1550-nm Uplink Channel	4
2.1.1 Optical Budget for 1550-nm Channel for the 104-km Demonstration ..	6
2.1.2 Present Optimum Performance of 1550-nm Channel	7
2.2 1300-nm Downlink Channel	7
2.2.1 Optical Budget for 1300-nm Channel for the 104-km Demonstration ..	8
2.2.2 Present Optimum Performance of 1300-nm Channel	8
2.3 Summary of the Optical Budget Analyses	8
3.0 WDM ISOLATIONS	9
4.0 ULTRASENSITIVE, LOW-BANDWIDTH FIBER-OPTIC RECEIVER	10
4.1 Summary	10
4.2 Introduction	10
4.3 Background	10
4.4 Approach	12
4.5 Description	13
5.0 MANCHESTER ELECTRONICS	16
5.1 Background	16
5.2 Manchester Encoder	16
5.3 Manchester Decoder	19
6.0 PFM HARDWARE ALTERATIONS	22
6.1 Introduction	22
6.2 Receiver Operating Characteristics	22
6.3 Pulse Width Requirements	25
6.4 Hardware Implementation and Results	26
7.0 AVALANCHE PHOTODIODE (APD) RECEIVER	28
7.1 Introduction	28
7.2 Theoretical Sensitivity Analyses	29
7.2.1 Noise Equations	29
7.2.2 Sensitivity Predictions	31
7.2.3 Summary of Theoretical Analyses	35
7.3 APD Receiver Design and Production	35
7.3.1 Introduction	35
7.3.2 Comparison of Performance Between PIN-FET and APD	35

7.4	Amplifier Design	36
7.4.1	Introduction	36
7.4.2	Purpose of Cascode Design	37
7.4.3	ACNAP Circuit Analysis	40
7.4.4	Use of Surface Mount Resistor as Transimpedance Feedback	40
7.5	Temperature-compensated Bias and Automatic Gain Control	42
7.5.1	Introduction	42
7.5.2	Circuit Function	42
7.5.3	Automatic Gain Control Interface	42
7.5.4	Temperature-Compensated Voltage Regulator	42
7.5.5	Adjustment of Temperature Control	43
7.6	Filter Design	43
7.7	Experimental Results	43
7.7.1	APD Receiver Bandwidth	43
7.7.2	APD Receiver Sensitivity	45
7.7.3	Testing of Temperature-Compensated Bias Control Circuit	46
7.7.4	Receiver Dynamic Range Using the PFM AGC	47
8.0	EMERGING TECHNOLOGIES	48
8.1	Fiber Amplifiers	48
8.2	Distributed-Feedback Laser Transmitters	50
9.0	CONCLUSIONS	50
10.0	REFERENCES	52

FIGURES

1.	Duplex standoff range versus spectral width.	3
2.	Optical diagram of long-distance repeaterless duplex link.	5
3.	Block diagram of ultrasensitive 19.2-Kbaud front-end.	12
4.	Ultrasensitive 19.2-Kbaud fiber-optic front-end.	14
5.	Block diagram of Manchester encoder.	17
6.	Electronic schematic of Manchester encoder.	18
7.	Block diagram of Manchester decoder.	20
8.	Electronic schematic of Manchester decoder.	21
9.	Receiver operating curves, S/N versus C/N, for 66-MHz PFM decoder.	23
10.	Receiver operating curves, S/N versus C/N, for 20-MHz PFM decoder.	24
11.	Comparison of PFM decoder threshold characteristics, 20- and 66-MHz RF bandwidth.	24
12.	Determination of PFM pulse width.	26

13. Block diagram of PFM encoder.	27
14. Block diagram of PFM decoder.	28
15. Peak sensitivity versus APD gain at various pre-amp noise values. (C/N = 16 dB, 50 MHz).	32
16. Dark current and gain versus bias voltage for RCA APD.	33
17. Dark current versus gain for RCA APD.	34
18. Noise current versus gain for RCA APD.	34
19. Normalized carrier and noise powers at the APD receiver.	35
20. Avalanche photodiode/transimpedance amplifier block diagram.	38
21. Avalanche photodiode/transimpedance amplifier with temperature-compensated bias and gain controller.	39
22. ACNAP amplifier schematic representation, using ACNAP component markings. ...	41
23. Frequency response of APD receiver: ACNAP model and measured -3 dB point. ...	44
24. Theoretical and measured sensitivities for the PIN-FET and APD receivers.	46
25. Optical diagram of an erbium-doped fiber preamplifier.	49

TABLES

1. Summary of system improvements	i
2. Channel range summary.	9
3. Measured performance data for new PIN-FET.	27
4. Measured performance data for RCA InGaAs APD.	45
5. Results of temperature-compensated bias circuit testing.	47

1.0 SYSTEM-LEVEL CONSIDERATIONS

The demonstration system is bidirectional, full duplex, over a single fiber. For discussion purposes, the duplex system is divided into two channels, the uplink and the downlink. The uplink channel carries high-bandwidth PFM-encoded video data at an optical wavelength of 1550 nm. The downlink carries low-bandwidth, Manchester-encoded control data at 1300 nm. Improvements were made to each channel. Extended repeaterless standoff range is the result of these improvements. Each channel is analyzed independently, but the actual duplex system standoff range is set by the shorter of the two channel lengths.

1.1 IMPACTS OF LASER PARAMETERS ON STANDOFF RANGE

At the transmitter end of each channel, changes in the laser parameters impact the standoff range. These changes are discussed in this section. Improvements to the receivers are detailed in later sections. The transmitter parameters that affect standoff range are laser output power, spectral width, and risetime. In the loss-limited regime higher output power extends the standoff range. Each decibel of increase adds 2 to 3 km to the 1300-nm channel and 4 to 5 km to the 1550-nm channel. In the bandwidth-limited regime, reductions in laser spectral width and transmitter risetime increase fiber bandwidth and extend the dispersion-limited length.

1.1.1 Loss-Limited Standoff Range

Improvements in output powers for both the 1300- and 1550-nm laser transmitters resulted in increased standoff range. The greatest gain occurred with the 1300-nm laser. The previous laser transmitter made by PCO had a +2.4-dBm peak output. The latest transmitter supplied by Laser Diode Inc., has +9-dBm peak output power. This 6.6-dB gain in output power translates to roughly 15 km additional range for the 1300-nm channel using the typical 0.45-dB/km attenuation reported for dispersion-shifted fiber. A modest gain of only 0.5 dB was obtained with the new 1550-nm laser.

An extensive search was performed to find more powerful 1300- and 1550-nm transmitters. Several manufacturers supply high-power laser diode modules. However, the requirement for a complete transmitter package, with drive electronics, bias and temperature feedback control, and thermoelectric cooler, reduces the field of suppliers considerably. At present no company offers a complete 1550-nm transmitter with output power greater than +1 dBm.

One company offers extremely high-output powers but only in module packages. OKI* sells a 1300-nm laser diode module with 20 mW (+13 dBm) and a 1550-nm module with 10 mW (+10 dBm) of peak power coupled to a single-mode fiber pigtail. These high powers are achieved by driving the lasers with currents of 350 to 400 mA compared to 50 to 100 mA for typical laser diodes. At first glance these lasers seem very attractive for long-distance applications. However, the OKI lasers have 10-nm spectral widths compared to 2 to 4 nm for typical Fabry-Perot lasers. This broad spectrum is unacceptable for long-distance, high-bandwidth links. At 10-nm width, the 1550-nm channel would be dispersion-limited to about 50 km.

Use of the OKI lasers for both channels would shift the duplex system range from loss-limited at 1300 nm to dispersion-limited at 1550 nm. Dispersion is not an issue at 1300 nm since a very low data rate is used. The current loss-limited range can be improved by using a higher power 1300-nm transmitter. If the full power available from a 1300-nm OKI laser, +13 dBm, was used in the

* OKI Semiconductor, 650 North Mary Avenue, Sunnyvale, CA 94086, (408) 720-1900.

demonstration system, an additional 4 dB in loss margin could be obtained. As noted, the OKI lasers are not available in complete transmitter packages to date. Perhaps a joint effort can be made: installing a high-power laser into another manufacturer's transmitter.

The 104-km range used in the previous report (Brininstool, 1987) was achieved from the concatenation of ten 10.4-km fiber segments, using fusion splices. The demonstration verified the capability of transmitting data over 100 km of actual fiber. No attenuators were used to simulate distances beyond the 104 km. For this report, an attenuator is inserted in-line with the existing 104 km of fiber to extend the effective range. Based on a specified fiber attenuation, the attenuator loss is directly converted to a corresponding fiber length. This is done for both wavelengths.

While the attenuator is an acceptable instrument for simulating additional length in the power regime, it does nothing for dispersion simulation. Analyses have been carried out to predict the maximum dispersion-limited range for the system. This is discussed in detail in the next section.

1.1.2 Bandwidth-Limited Standoff Range

It is important to consider the factors that limit the system standoff range in the bandwidth regime. This is done independently for both channels of the duplex link. The 1300-nm channel operates at 19.2 Kbps. It is not necessary to analyze this channel, since it will never cause the system to be bandwidth limited. The high-bandwidth 1550-nm channel is fully considered.

Several factors affect the ultimate bandwidth-limited standoff range for the 1550-nm channel. These are the magnitudes of the component risetimes, laser spectral width, fiber chromatic dispersion, and system bandwidth. For a given system, employing single-mode fiber, the laser spectral width impacts the dispersion-limited length directly. Since a single-mode fiber is used, the only limiting mechanism in the fiber is chromatic dispersion, which is the sum of material and waveguide dispersion. To first order, no pulse broadening from modal distortion exists. The bandwidth of the fiber decreases linearly with increases in length. The term dispersion-limited is used interchangeably with bandwidth limited.

Two system equations are used to evaluate bandwidth limitations. The first relates the system risetime to the individual component risetimes:

$$t_{sys}^2 = t_{TX}^2 + t_{fiber}^2 + t_{RX}^2 \quad (1)$$

where t_{sys} is the total system electrical risetime
 t_{TX} is the transmitter electrical risetime
 t_{fiber} is the fiber equivalent electrical risetime
 and t_{RX} is the receiver electrical risetime.

The second equation gives the fiber equivalent electrical risetime:

$$t_{fiber} = M\Delta\lambda L \quad (2)$$

where M is the total chromatic dispersion of the fiber
 $\Delta\lambda$ is the full width half maximum (FWHM) spectral width of the laser transmitter
 and L is the fiber length or standoff range.

By combining the two equations and inserting the various component parameter values, a relationship between laser spectral width and standoff range is derived. The following values are used:

System bandwidth: 50 MHz System risetime: 7 ns
 Transmitter risetime (from typical data sheets): 1 ns
 Receiver bandwidth: 60 MHz Receiver risetime: 5.83 ns

For dispersion-shifted fiber, the chromatic dispersion is ≤ 2.7 ps/nm-km at 1550 nm.

From these values, a linear relationship between spectral width and dispersion-limited standoff range is found:

$$\Delta\lambda L = 463 \text{ nm-km} \quad (3)$$

A bandwidth safety factor of 3 is used for this result. That is, the fiber risetime used for design purposes is set at one-third the fiber risetime found from the equations. This provides sufficient safety margin for uncertainties of the component parameter values. As an example of applying the relationship, if a 3-nm laser is used, typical of a Fabry-Perot multilongitudinal-mode laser, the dispersion-limited length is 155 km. A plot of the standoff range as a function of spectral width fully illustrates the result. This is shown in figure 1.

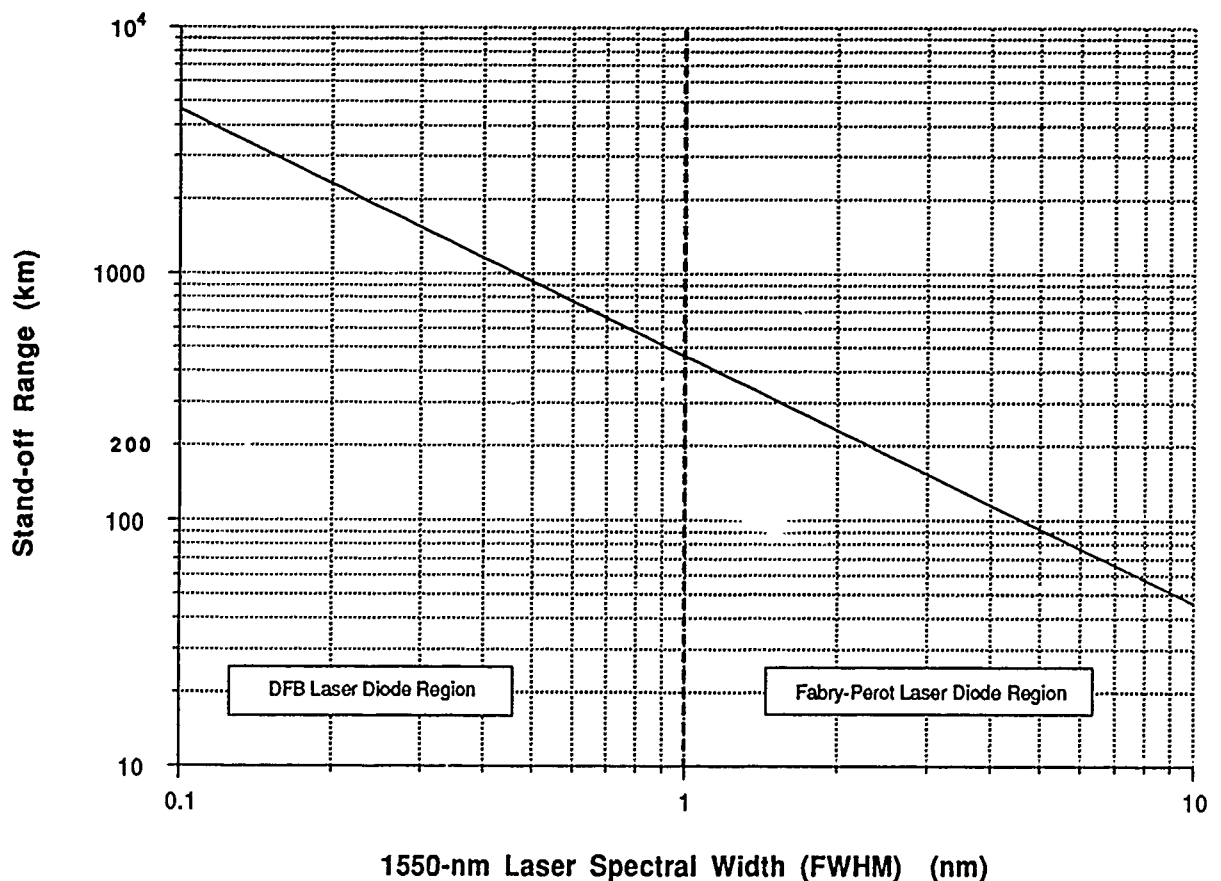


Figure 1. Duplex standoff range versus spectral width.

Figure 1 is divided into two regions of laser spectral width. In practice, the dividing line between the two types of lasers is not distinct, but for purposes of discussion was chosen at 1 nm. A laser diode with a spectral width of 1 nm or less is a distributed feedback (DFB) type and for 1 nm or greater it is a Fabry-Perot type. From the plot it is seen that the dispersion-limited length for a Fabry-Perot laser diode is about 463 km.

Another useful parameter taken from the above equations is the equivalent electrical fiber bandwidth as a function of laser spectral width and fiber length. For dispersion-shifted fiber this relationship is

$$BW_{\text{fiber_elec}} = \frac{(130 \text{ GHz} - \text{nm} - \text{km})}{\Delta\lambda L} \quad (4)$$

Equation 4 applies to any system and component bandwidths. For example, if a 200-km system uses a 2-nm laser transmitter, the fiber's electrical bandwidth is roughly 325 MHz. This bandwidth is then used to specify the ultimate system bandwidth attainable.

A spectral width value of 1 nm pushes the limits of performance for Fabry-Perot laser diodes. Measurements reveal widths of 2 to 4 nm, which convert to 116- to 231-km ranges. To achieve a 200-km standoff range and maintain a bandwidth safety factor of 3, the laser spectral width must not exceed 2.3 nm. It is apparent from the implementation of the improvements discussed in this report that transition to a DFB laser transmitter for the 1550-nm channel is warranted. The DFB allows expansion in range or system bandwidth. Other advantages of upgrading to a DFB laser are discussed in the emerging technology section at the end of the report.

2.0 OPTICAL POWER BUDGETS

This section details complete optical power budgets for both 1300- and 1550-nm channels. Included in each budget are laser power output, receiver sensitivity, fiber attenuation, splice loss, wavelength division multiplexer (WDM) insertion loss, and safety factor. The budgets allow calculation of present and predicted performance of the system in the loss-limited regime. Given values for the various parameters, either by assumption of typical values, by using actual measured values, or by predictions of state of the art, the maximum allowable standoff range is obtained. Of course any other parameter besides range can be allowed to be the unknown. For instance, the minimum-allowable fiber attenuation can be specified from the budgets if a standoff range is selected. Similarly, the minimum-allowable receiver sensitivity is found given specified values for parameters such as range, attenuation, and laser output power. Sensitivity is indirectly valuable in determining the ultimate system bandwidth capacity. The system design procedure is iterative, and the budgets are at the heart of the process.

2.1 1550-nm UPLINK CHANNEL

It is helpful to begin the optical budget discussion with the performance of the uplink channel discussed in the 104 .n report. This serves as a baseline. An optical power budget helps detail the various component values for that demonstration. Next the present-day level of performance is noted. Finally, projections of future performance are considered. As an aid, the optical block diagram for the duplex link is given in figure 2.

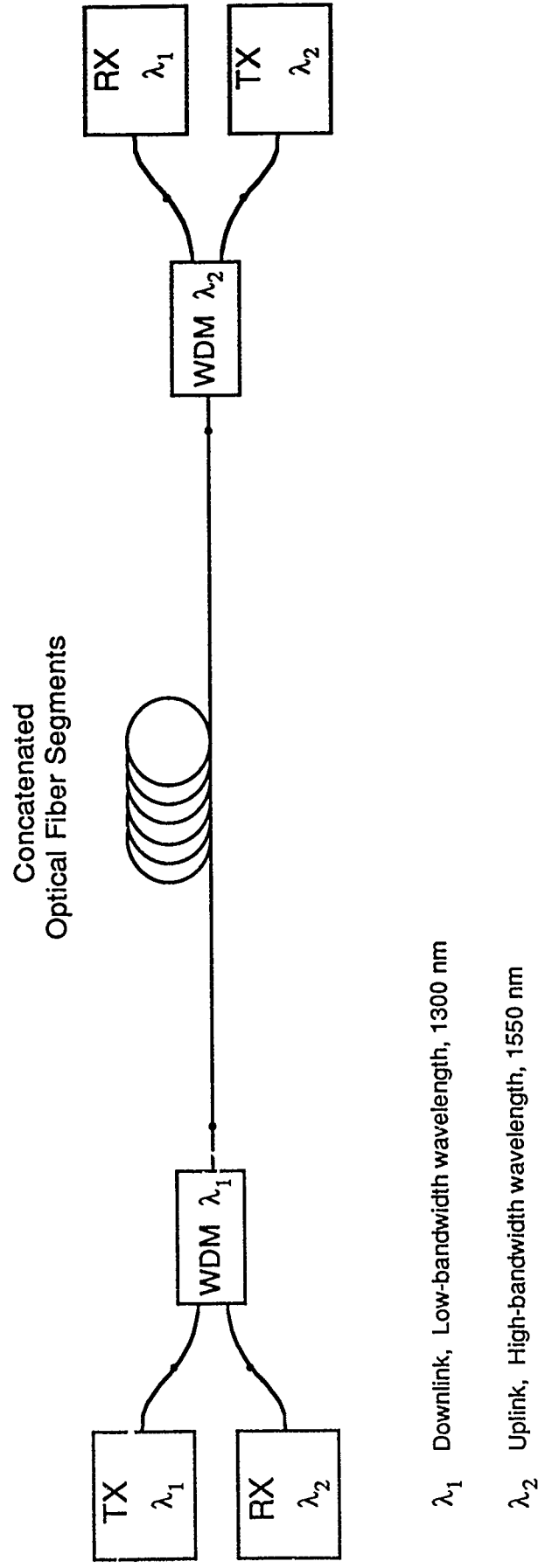


Figure 2. Optical diagram of long-distance repeaterless duplex link.

2.1.1 Optical Budget for 1550-nm Channel for the 104-km Demonstration

From the optical diagram, the power budget equation is written as follows:

$$P_{tx} - P_{rx} = \Sigma \text{Losses} = \alpha NL + (N + 3)l_{sp} + 2l_{wdm} + l_{safety} \quad (5)$$

where

P_{tx} is the peak output power (dBm) from the laser transmitter

P_{rx} is the peak receiver sensitivity (dBm) at the required carrier-to-noise ratio

Σ Losses is the sum of all component losses between transmitter and receiver in dB:

α is the optical fiber attenuation in dB/km

N is the total number of spliced segments of fiber cable

L is the length of each cable segment

l_{sp} is the average splice loss

l_{wdm} is the insertion loss of each WDM

and l_{safety} is the safety margin added to the budget to guard against component value uncertainties, system degradations, environmentally induced loss variations, and repairs.

From equation 5 the maximum standoff range, NL , is found. Fiber cables are presently available in maximum segment lengths of 25 km. For the exact range, minor adjustments are made due to nonintegral solutions of N . For instance, a solution of $N = 5.5$ is equivalent to a link made up of five complete 25-km sections plus almost half of an additional section. The power budget equation does not account for the extra splice required to add the last length of fiber. In most cases the splice loss can be neglected, since a 0.1-dB splice amounts to less than half a kilometer of fiber loss.

Previous parameter values for the 104-km demonstration:

1550-nm transmitter output power (peak)	P_{tx}	-0.5 dBm
PIN-FET receiver sensitivity (peak)	P_{rx}	-45.75 dBm
Total margin	$P_{tx} - P_{rx}$	45.25 dB

Before continuing, a word is necessary concerning the specified value of peak receiver sensitivity. Since the majority of fiber-optic applications are digital, receiver manufacturers typically specify sensitivity at a given bit error rate (BER). The industry standard is a $BER = 10^{-9}$. From Gaussian-noise statistics and assuming a thermal-noise-limited receiver, this BER occurs for a carrier-to-noise ratio (C/N) of 21.5 dB (Yariv, 1976). The PFM encoding is analog and for the demonstration requires a $C/N = 16$ dB. The sensitivity must be adjusted accordingly. In addition, manufacturers specify sensitivity as the *average* value of power necessary for a $BER = 10^{-9}$. This is probably because the average value is easier to measure and also perhaps, from a marketing stand point, it appears better! The underlying assumption made is that the average value is measured under test conditions where the input signal to the receiver is a pseudo-random nonreturn to zero (NRZ) bit stream with an average duty cycle of 50%. To be meaningful in a digital budget analysis, one adds 3 dB to the average receiver sensitivity so it can be accurately compared next to the value of laser transmitter output, most commonly given as peak power (marketing?). For example, for the 50-MHz PIN-FET used in the original 104-km system, the average sensitivity was -46 dBm. Thus, the peak sensitivity is -43 dBm, at a $C/N = 21.5$ dB. However, the peak sensitivity of the PIN-FET for the PFM receiver ($C/N = 16$ dB) is 5.5 dB electrical (2.75 dB optical) better or -45.75 dBm.

Previous component losses at 1550 nm for the 104-km demonstration:

WDM insertion losses	21_{wdm}	1.3 dB
Splice losses (0.43 dB per splice)	1_{sp}	$(N + 3) 0.43 \text{ dB}$
Fiber loss (0.25 dB/km, 25-km segments, N segments) αNL		$6.25 N \text{ dB}$
Safety factor	1_{safety}	5 dB

Substituting these values available for the 104-km link gives the following power budget equation:

$$-0.5 \text{ dBm} - (-45.75 \text{ dBm}) = (0.25 \text{ dB/km}) (25 \text{ km})N + (N + 3) (0.43 \text{ dB}) + 1.3 \text{ dB} + 5 \text{ dB}$$

Solving for the number of 25-km fiber segments N :

$$N = 5.64.$$

The approximate 1550-nm channel standoff range was then 141 km. As was noted in the 104-km report (Brininstool, 1987), it was the 1300-nm channel that ultimately limited the system standoff range to 115 km. This was due mainly to the higher fiber attenuation at 1300 nm. This is detailed in the 1300-nm budget section of this report. Since that report was published, improvements in both channels have been realized. Presently, for the 1550-nm channel, a slightly higher-power laser transmitter has been installed, emitting 0.0-dBm peak, for a gain of 0.5 dB. More importantly, the 1550-nm receiver sensitivity has been improved by a factor of 6 dB. This was achieved in two ways. First the PIN-FET receiver was replaced with an avalanche photodiode (APD) receiver. The APD has internal gain which provides detection of lower incident optical signal levels. This improvement provided 4 dB better performance over the PIN-FET. Second, the PFM transmitted pulse width was changed from 12 to 16 ns. This allowed the receiver bandwidth to be reduced to 32 MHz from the previous 50 MHz and added 2 dB more to the sensitivity. Together, the changes in the transmitter and receiver added 6.5-dB gain to the total optical loss margin. This translates to an additional 24 km and the total range is then 165 km.

2.1.2 Present Optimum Performance of 1550-nm Channel

Note, from the component loss list, that the present 1550-nm channel standoff range has been calculated for a fiber attenuation of 0.25 dB/km and a splice loss of 0.43 dB. The attenuation is the value guaranteed by the manufacturer and is conservative. Measured attenuations from the 104-km demonstration were 0.212 dB/km. These values were for a loose-tube buffered fiber, which was used to minimize excess microbend attenuation. The high splice losses were due to the difficulty of splicing fiber in a loose tube and from using an unsophisticated fusion splicer. Splice losses are typically 0.1 dB. For optimum, the WDM losses are set to 0.75 dB each, slightly higher than previous levels to account for potentially higher losses from the additional isolation required. Incorporating all of these improvements into the system gives a new power budget for the 1550-nm channel:

$$0 - (-51.75) = (0.215 \text{ dB/dm}) (25 \text{ km})N + (N + 3) (0.1 \text{ dB}) + 1.5 \text{ dB} + \text{dB}$$

So $N = 8.2$. This converts to a standoff range of 205 km under optimum conditions.

At distances of this magnitude one can see the importance of adding a hefty safety factor to the analysis. As an example, at 200 km a tolerance of only $\pm 0.01 \text{ dB/km}$ in fiber attenuation alters the available power at the receiver by $\pm 2 \text{ dB}$. Seen another way, a 2-dB variation at 0.215 dB/km is equivalent to over 9 km of fiber. The 5-dB safety factor accounts for uncertainties such as these.

2.2 1300-nm DOWNLINK CHANNEL

Similar to the 1550-nm channel analysis, an optical budget is generated for the 1300-nm channel. The budget for the 104-km system is used again as the baseline. The power budget equation is similar, the component values change.

2.2.1 Optical Budget for 1300-nm Channel for the 104-km Demonstration

Previous parameter values for the 104-km demonstration:

1300-nm transmitter output power (peak)	P_{tx}	+2.4 dBm
PIN-FET receiver sensitivity (peak)	P_{rx}	-59.0 dBm
Total margin	$P_{tx} - P_{rx}$	61.4 dB

Since this is a digital system no adjustment is made in the sensitivity. The -59 dBm is peak sensitivity at BER = 10^{-9} assuming a 50% average duty cycle as measured by the manufacturer.

Previous component losses at 1300 nm for the 104-km demonstration:

WDM insertion losses	21_{wdm}	1.2 dB
Splice losses (0.43 dB per splice)	1_{sp}	$(N + 3) 0.43$ dB
Fiber loss (0.45 dB/km, 25 km segments, N segments) αNL		$N \times 11.25$ dB
Safety factor	1_{safety}	5 dB

Substituting these values available for the 104-km link gives the following equation:

$$+2.4 \text{ dBm} - (-59 \text{ dBm}) = (0.45 \text{ dB/km}) (25 \text{ km})N + (N + 3) (0.43 \text{ dB}) + 1.2 \text{ dB} + 5 \text{ dB}$$

Solving for the number of 25-km fiber segments N :

$N = 4.61$. The maximum standoff range is then computed as 115 km. As is seen, for the original demonstration, the 1300-nm channel limited the total system standoff range to 115 km.

Improvements in the 1300-nm channel extend this range. As with the 1550-nm channel, the significant changes were on the transmitter and receiver. A higher-power 1300-nm laser transmitter is now employed. It has a peak output power of 8 mW or +9 dBm compared to +2.4 dBm for the previous laser. This provides an additional 6.6 dB to the margin. The receiver performance has been greatly enhanced. The PIN-FET is replaced with an ultra-low-noise receiver using a PIN photodiode coupled to a high-impedance integrating preamplifier. The measured sensitivity is -73 dBm average compared to -62 dBm for the PIN-FET. This improvement adds another 11 dB to the margin. The total margin improvement from these two changes is 17.6 dB! Applying these values to the optical budget yields the present 1300-nm range of 153 km.

2.2.2 Present Optimum Performance of 1300-nm Channel

Here again the value for attenuation of 0.45 dB/km at 1300 nm is that specified by the manufacturer. Actual measured attenuation at 1300 nm for 100 km of fiber in a loose-tube cable averaged 0.384 dB/km. Applying the new laser and receiver performance and using a 0.384-dB/km attenuation, a 0.1-dB splice loss, and a 0.75-dB WDM loss give the optimum loss budget as:

$$+9 - (-70) = (0.384 \text{ dB/km}) (25 \text{ km})N + (N+3) (0.1 \text{ dB}) + 1.5 \text{ dB} + 5 \text{ dB}$$

So $N = 7.44$. This translates to a range of 186 km.

2.3 SUMMARY OF THE OPTICAL BUDGET ANALYSES

The following table summarizes the channel ranges at the 104-km report stage, the present stage, and the present optimal stage. Again note that the actual duplex system standoff range is limited to the shorter of the two channel ranges, in this case, the 1300-nm channel range.

Table 2. Channel range summary.

Stage of Development	1300-nm Channel Range	1550-nm Channel Range
104-km demonstration	115 km	141 km
Present	153 km	165 km
Present optimum	186 km	205 km

Work is planned for the second and third quarters of FY 91 that will extend the 1550-nm channel range dramatically. Use of an erbium-doped fiber amplifier (EDFA) as a preamplifier at the receiver promises to increase the sensitivity by at least 10 dB! These amplifiers have only recently been available for off-the-shelf use. Fiber amplifiers will have considerable impact on all long-distance links, both submarine and terrestrial. They will allow huge increases in repeater spacing and, perhaps more importantly, they offer potentially lower cost, lower power consumption, and higher reliability than the opto-electronic repeaters used presently. A discussion on this subject is presented in a later section.

3.0 WDM ISOLATIONS

As the standoff range increases, so does the required level of isolation for the WDMs. For the 104-km demonstration, the 1300-nm WDM required a minimum isolation of 46 dB and the 1550-nm WDM needed better than 66 dB. New calculations are performed for WDM isolations for a 200-km system. The calculation involves predicting the incident power at the receiver from the in-band signal given a 5-dB safety factor and comparing this to the unwanted out-of-band power incident at the same receiver if no WDM is present. Then a WDM is inserted that lowers the the unwanted signal power 11 dB below the minimum receiver sensitivity. The amount needed by the WDM to lower this power is the isolation. The reader is referred to the 104-km report for more details on this calculation.

For the new 200-km system WDMs, the following assumptions are made:

1330-nm laser output power	+9	dBm peak
1550-nm laser output power	0	dBm peak
Attenuation at 1300 nm	0.45	dB/km
Attenuation at 1550 nm	0.25	dB/km
Splice loss	0.1	dB
Safety factor	5.0	dB
WDM insertion loss	0.75	dB each
Segment length	25	km

The results of the calculations show that the 1300-nm WDM, the one isolating the 1300-nm transmitter from the 1550-nm receiver, requires a minimum of 80 dB isolation. The 1550-nm WDM requires a minimum of 100 dB. Presently, the WDMs in use have isolations greater than 95 dB for both 1300- and 1550-nm WDMs as measured by the manufacturer. It is planned that a new set of upgraded WDMs will be installed in the system during FY 91.

4.0 ULTRASENSITIVE, LOW-BANDWIDTH FIBER-OPTIC RECEIVER

4.1 SUMMARY

An ultrasensitive, low-bandwidth, fiber-optic receiver is described that is designed to receive a Manchester-encoded digital data signal at an asynchronous signaling rate of 19,200 baud. The receiver consists of a ternary, unity-gain PIN photodiode operated in the photovoltaic mode, coupled to an integrating preamplifier consisting of a low-noise silicon JFET operated in a cascode topology. The preamplifier stage is followed by a differentiator, which restores a flat passband to the preamplifier, and an active, third-order Bessel-aligned low-pass filter, which provides the optimum amplifier bandwidth to pass the Manchester-encoded digital data with constant group delay. The preamplifier is designed to operate in an active, low-noise mode under weak signal conditions and to limit gracefully at high signal levels, clipping symmetrically to pass the 50% duty cycle Manchester-encoded signal without introducing any errors. This feature eliminates the requirement to incorporate an automatic gain control (AGC) loop within the front-end to provide a high receiver dynamic range.

The calculated and experimentally verified average optical sensitivity for the fiber-optic receiver is -73 dBm at receiver threshold (corresponding to a BER of approximately 10^{-9} errors/bit). This corresponds to an improvement of 11 dB in optical sensitivity over a receiver based upon a commercial PIN-FET detector. The measured dynamic range of the reported receiver is in excess of 76 dB (the dynamic range measurement is actually limited by the maximum optical power available from the $1.3\text{-}\mu\text{m}$ laser transmitter!). To the best of our knowledge, -73 dBm corresponds to the highest sensitivity ever reported for a fiber-optic receiver operating at this data rate.

4.2 INTRODUCTION

This chapter describes an ultrasensitive fiber-optic receiver designed at Naval Ocean Systems Center (NOSC) for use in a long-haul, full-duplex fiber-optic communications system demonstration. In this demonstration system a digital, Manchester-encoded, asynchronous signal at 19,200 baud (RS-232 format) is transmitted for as great a distance as possible within the current state of the art without the use of optical repeaters over a span of dispersion-shifted single-mode optical fiber at an optical wavelength of $1.30\text{ }\mu\text{m}$. The lower-loss, $1.55\text{-}\mu\text{m}$ optical window is used for simultaneous transmission of a higher bandwidth video signal propagating in the opposite direction over the same optical fiber. Because a high-power, state-of-the-art injection laser transmitter is, by definition, already employed as the $1.3\text{-}\mu\text{m}$ transmitting source, little can be accomplished to increase the operational range of the system by increasing the transmitter power level. The optical fiber attenuation and fusion splice insertion losses are also at the practical minimum possible values at this wavelength. Improving the sensitivity of the optical receiver is, therefore, the only practical approach possible for increasing the maximum repeaterless communications range of the demonstration system.

4.3 BACKGROUND

The demonstration link initially employed a commercial PIN-FET module to receive the $1.3\text{-}\mu\text{m}$ digital command-control signal. The PIN-FET incorporates a feedback (transimpedance) resistor selected to provide an overall detector bandwidth of 1 MHz. This value of feedback resistor corresponds to the highest value of resistance available for the module, according to the manufacturer, as further increases in the magnitude of the feedback resistor would only serve to limit the receiver

bandwidth but not reduce the overall preamplifier noise because the dominant noise generator is the gallium arsenide (GaAs) FET gain block—not the transimpedance resistor at bandwidths less than 1 MHz.

Using the PIN-FET as the front-end of a digital receiver, it was found that the limiting communications channel margin corresponded to the low bandwidth command/control channel operating at 1.30 μm . Considerably higher transmission distance was available over the duplex 1.55- μm video channel due to the optical fiber's lower attenuation within the 1.55- μm optical window, which more than offsets the reduced receiver sensitivity at the video bandwidth. Any improvements in the operating margin at the 1.30- μm wavelength, therefore, will permit a corresponding increase in the link's duplex operating range.

The measured average sensitivity of the commercial PIN-FET-based optical receiver was -62 dBm when receiving a 19,200-baud Manchester-encoded data signal. For this measurement, the PIN-FET was followed by a 20-KHz lowpass filter to remove out-of-band noise components. Surprisingly, the measured sensitivity at 19,200 baud was only slightly better than the specified performance for the module when receiving a 1-MBps data signal. If the noise generated within the PIN-FET module had been spectrally white, its root mean square (RMS) magnitude should have been reduced by the square root of the ratio of the postdetection filter bandwidth from the detector (the signal bandwidth from the module before filtering was 1 MHz and after filtering was 20 KHz, to allow for passage of a Manchester-encoded 19.2-Kbaud signal) and the bandwidth of the lowpass filter following the PIN-FET module. $(20 \text{ KHz}/1 \text{ MHz})^{1/2} = 0.141$ or -17.2 dB, electrical (corresponding to an improvement in sensitivity of -8.6 dB, optical). Less than a 1-dB sensitivity improvement was actually realized, implying that following the output of the PIN-FET module with a three-pole Bessel low-pass filter optimized for a bandwidth of 20 KHz had a negligible effect upon the output noise. This result indicated that the GaAs FET noise was predominantly $1/f$ in nature. This fact was subsequently confirmed with a spectrum analyzer.

In retrospect, the poor performance of the PIN-FET when receiving a low bandwidth digital signal should not have been particularly surprising, as virtually no commercial applications use GaAs FETs at such low frequencies. For example, a typical TELECOM fiber-optic receiver application includes a highpass filter (perhaps in the form of blocking capacitors) that greatly attenuates $1/f$ noise from the GaAs FET without affecting a high-data-rate signal adversely, which might correspond to bandwidths of 10s or even 100s of MHz. Unfortunately, our much lower bandwidth Manchester-encoded 19.2-Kbaud signal lies entirely within the spectral region where it would be attenuated by such a high-pass filter as well.

The problem with a PIN-FET module in this application, basically, is that GaAs FETs are not useful at audio frequencies because they exhibit high $1/f$ noise compared to silicon devices and their very high gain-bandwidth product is of lesser importance at audio frequencies than at radio frequency (RF) or microwave frequencies. A quick survey of the literature determined that silicon devices, in general, and large surface area JFETs, in particular, have far superior $1/f$ noise characteristics compared to GaAs FETs at low frequencies, at the expense of gain-bandwidth product, of course.

One silicon JFET in particular, the industry standard CM860/2N6550 used in applications such as phono and tapehead preamplification, strain gage, and biomedical applications, has extremely good low frequency $1/f$ noise characteristics but correspondingly high junction capacitances. Under most high-gain circuit topologies, the very high drain to gate capacitance of the device negates any advantage of using it to amplify a signal from a high impedance source such as a photodiode, since the resulting Miller capacitance bypasses the signal to ground at even the low audio frequencies of interest. The use of a cascode circuit topology, however, in which the first stage exhibits unity voltage gain, effectively eliminates the Miller capacitance at the expense of increased circuit complexity. It is

apparent that if a cascode circuit topology is employed to eliminate the Miller capacitance of the device, the excellent noise properties of the CM860/2N6550 make it a prime candidate for the active device in an ultrasensitive fiber-optic receiver front-end.

4.4 Approach

A transimpedance front-end using the CM860/2N6550 FET operated in conjunction with a Lasertron* QDEP-075 ternary photodiode having a high responsivity at a wavelength of $1.30\ \mu\text{m}$ was next analyzed. Figure 3 is a block diagram of the low-bit-rate receiver. Normally, PIN photodiodes are operated in the photoconductive mode (with reverse direct current (DC) bias) to minimize the photodiode's junction capacitance. This improves the frequency response of the photodiode at the expense of adding a shot-noise component from the dark current, which flows under reverse biased operation. At high-signal bandwidth, the added shot-noise component is negligible compared to the preamplifier noise; however this is not the case at audio frequencies if a very low noise preamplifier is used. Thus, it was decided to operate the photodiode in this receiver in the zero bias, or photovoltaic, mode to preclude the generation of detector dark current and the resulting shot noise that would otherwise reduce the receiver sensitivity. The reduced bandwidth of the photodiode due to the larger junction capacitance is not really much of a problem at the low data rate of interest, in any case. The circuit was modeled using ACNAP™ on a Macintosh II™ computer to optimize the magnitude of the feedback resistor. It was determined analytically that the sensitivity of such an optical receiver would be approximately $-68\ \text{dBm}$, with the source of noise dominated entirely by thermal noise generated by the transimpedance feedback resistor. The noise introduced by the JFET itself was determined to be totally negligible.

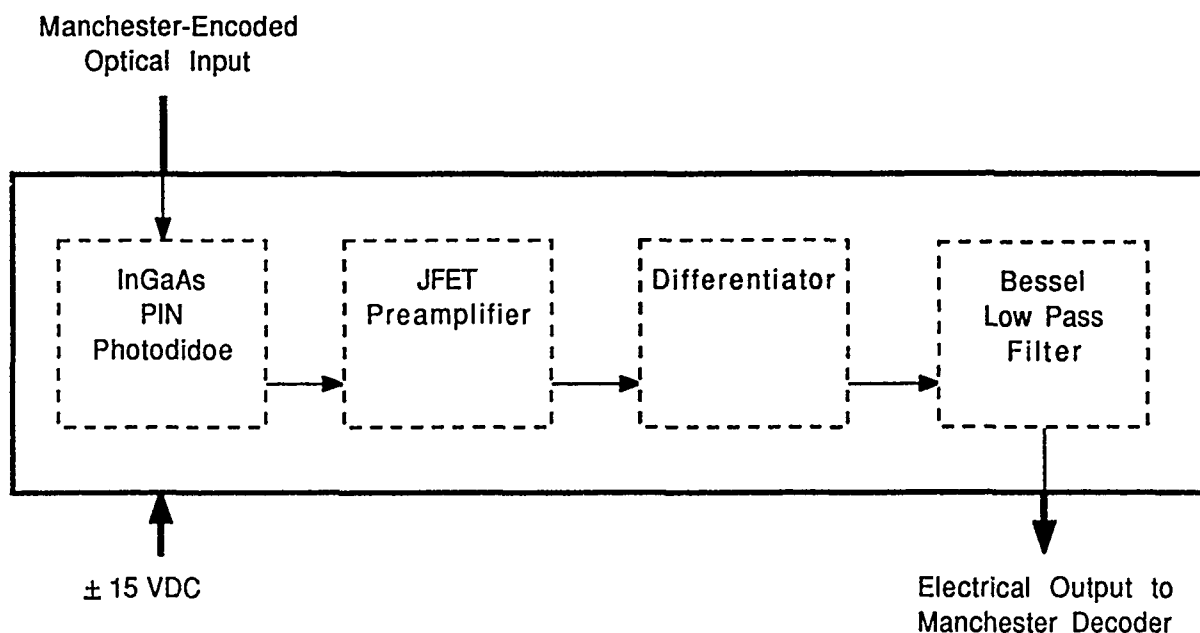


Figure 3. Block diagram of ultrasensitive 19.2 Kbaud front-end.

* Lasertron, 37 North Avenue, Burlington, MA, 01803, (617) 272-6462.

While the previous front-end design is clearly an improvement over the PIN-FET, increasing the obtainable optical receiver sensitivity by 6 dB, it is quite apparent that even more receiver sensitivity is available from this specific circuit topology if the primary noise source, the feedback resistor in this case, is eliminated from the design. Recall that the purpose of the feedback resistor in a trans-impedance preamplifier is to shorten the input time constant resulting from the parallel combination of the amplifier and photodiode shunt resistance and capacitance by the incorporation of shunt feedback within the circuit topology. Eliminating the feedback resistor, therefore, creates a long input time constant, which results in the time integral of the signal, not the signal itself, being output from the pre-amplifier. The elimination of negative feedback also results in a circuit that is unconditionally stable, not requiring any internal frequency compensation or shaping, which reduces the gain-bandwidth product of the forward amplification block. Due to the effective integration that occurs to the input signal as a result of the long input time constant of this type of photodiode front-end, such a "nonfeedback" preamplifier design is commonly referred to as an integrating front-end.

The same cascode silicon JFET-PIN detector combination operated without a feedback resistor was considered operating as an integrating front-end. This requires rethinking the signal processing chain slightly. Because the signal transfer function of such a preamplifier is not constant (flat)—its signal magnitude response rolls off over the frequency band of interest at a rate of -6 dB/octave—it is necessary to include a subsequent electronic equalizer having the inverse (a differentiating) response after the preamp (a slope of $+6$ dB/octave). It is also necessary in practice to include a lowpass filter to attenuate the response of the system to frequencies above the signal band of interest (above 20 KHz in this case). At very high frequencies the gain of a differentiator is very high and, therefore, it can contribute noise to the system if the output is not rolled off in some manner.

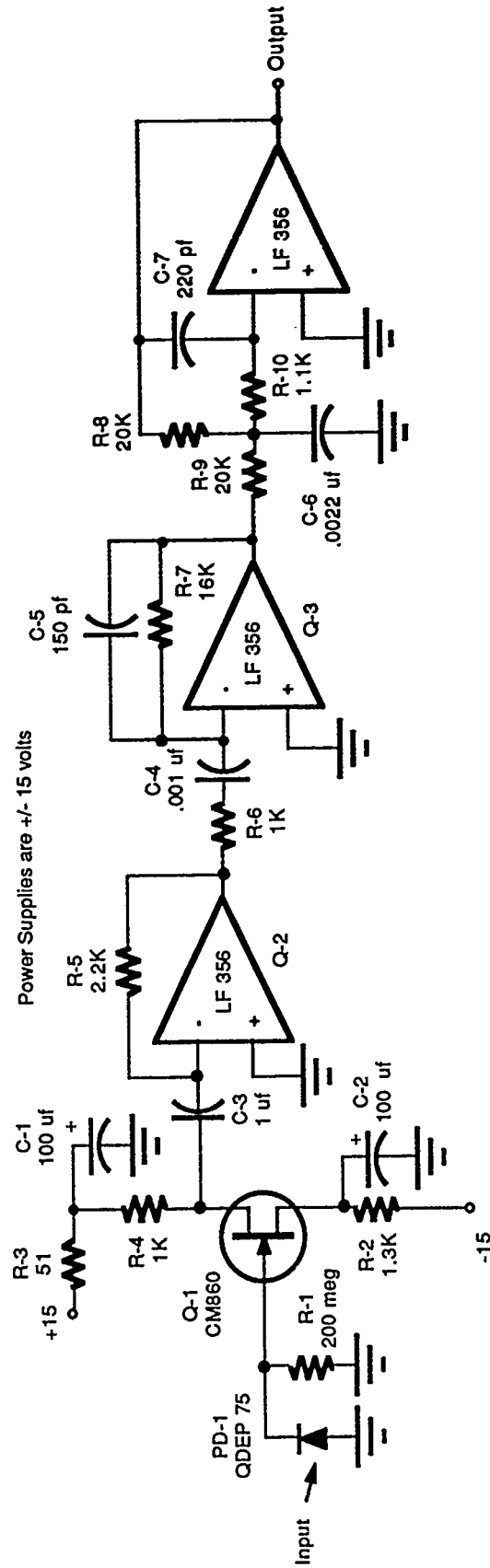
An ideal integrating receiver front-end has infinite input resistance (therefore no thermal-noise current contribution), its input impedance being completely capacitive in nature. It is necessary in practice to DC-bias the gate of a JFET, so a high-resistance biasing resistor must be included for this purpose. As the gate biasing resistance in parallel with the equivalent shunt resistance of the signal source (the ternary photodiode operated in the photovoltaic mode) is the dominant noise source in the integrating preamplifier, it is important to make its value as high as practically possible to minimize its thermal-noise contribution. The zero-voltage-biased shunt resistance of the ternary PIN photodiode selected for the receiver is nominally 200 megohms, so little sensitivity increase can be gained by using a gate biasing resistor significantly greater than 200 megohms because the preamplifier's biasing resistance appears in parallel with the photodiode's shunt resistance. An excessively large gate bias resistor would lead to a difficult-to-obtain device, stray printed circuit board resistance effects (a thin moisture film could easily have more conductivity than, say, a 1000-megohm resistor), and possibly bias instability with aging and temperature in the FET preamplifier. Using engineering judgment, 200 megohms was chosen as the gate biasing resistance for the JFET.

When a cascode-connected CM860/2N6550 JFET configured as an integrating front-end using a 200-megohm gate biasing resistor was analyzed in conjunction with the selected ternary PIN photodiode, a receiver optical sensitivity corresponding to a level of -73 dBm was predicted. The calculations were confirmed experimentally in the fiber-optic demonstration link using the actual receiver front-end circuit, which is described subsequently.

4.5 Description

The electronic schematic diagram for the ultrasensitive, low-bandwidth fiber-optic receiver is shown in figure 4. This section describes the receiver operation.

- Stage 1: PD-1, a Lasertron QDLP-75 ternary photodiode, is operated in the photovoltaic mode by maintaining its bias near-zero volts to eliminate dark current and the resulting



Stage 1: Photodiode Stage 2: Integrating Preamplifier Stage 3: Differentiator Stage 4: Low-Pass Filter

Figure 4. Ultrasensitive 19.2-Kbaud fiber-optic front-end.

shot-noise component. The JFET gate biasing resistor, R-1, serves to maintain the potential across PD-1 and the gate of JFET Q-1 to ground near-zero volts because no steady state current flows through it. A value of 200 M Ω was chosen for R-1 as a practical maximum consistent with minimizing the resistor's thermal noise contribution. At a resistance value of 200 M Ω the thermal noise current component contributed by R-1 is of the same magnitude as that from the zero biased shunt resistance of PD-1. Q-1 is a CM860/2N6550 ultra-low-noise silicon JFET biased to 10 mA by R-2 for maximum thermal stability. The combination formed by R-3 and C-1 and R-2 and C-2 form a decoupling network to prevent feedback to the first stage due to power supply modulation and the resulting "motor-boating" instability, which would be caused by the subsequent operational amplifier stages operating in a limiting mode at high optical signal levels.

- Stage 2: Q-2 is a low-noise operational amplifier operated as a transimpedance (current to voltage converter) stage that provides a near-zero load impedance for the drain of Q-1. Q-1 and Q-2 together effectively form a cascode gain block that negates Miller effect for the first stage, thereby minimizing the shunt capacitance presented to PD-1 by the input of the preamplifier. The transimpedance of this stage is set at a value of 2200 volts per amp by the value of R-5. C-3 is a blocking capacitor that prevents DC loading by the transimpedance stage from disturbing the DC operating point established for Q-1. R-4 is chosen to have a much larger impedance than the transimpedance stage, while still permitting DC-bias current to flow into Q-1 without causing excessive voltage drop; thus, virtually all of the signal current flows into the transimpedance amplifier rather than through R-4 to the power supply. The operational amplifiers (op-amps) chosen are BiFET LF-356s due to their low noise and graceful limiting characteristics when overdriven. Not all op-amps exhibit the freedom from latchup and symmetrical delay characteristics of the LF-356 when they are driven into overload. Symmetrical overload characteristics permit the preamplifier to pass a Manchester code when the active devices are saturated due to signal overload conditions.
- Stage 3: Capacitor C-4 acts as a differentiator that compensates for the integration that occurs to the signal current from PD-1 when it is applied to the high impedance capacitive node at the gate of Q-1. The inverse frequency compensation from the differentiator restores the amplified signal to the original shape it had prior to amplification by the integrating front-end. R-6 limits the gain of the differentiator at frequencies greatly in excess of the signal bandwidth, thereby minimizing out-of-band noise amplification by the differentiator. The combination of Q-3 and R-7 forms a second transimpedance amplifier having a transimpedance of 16,000 volts per amp, which provides the virtual ground required for proper operation of the differentiation network composed of R-6 and C-4. C-5 provides the real pole necessary to implement the three-pole Bessel lowpass filter response.
- Stage 4: The combination of R-8, R-9, R-10, C-6, and C-7 in conjunction with Q-4 serves to implement an "infinite gain block" active filter realization, which provides the remaining pair of complex poles necessary to generate the three-pole Bessel lowpass filter response for the fiber-optic receiver. The complex pole pair from the active filter is aligned with the real pole from stage 3 to result in the required 20-KHz frequency rolloff and linear phase characteristics necessary to provide optimum filtering for the 19.2-Kbaud Manchester-encoded signal. Optimum filtering is defined as that which achieves the maximum signal-to-noise ratio possible for a particular signal using a linear filter. Q-4 also provides a low impedance signal output suitable for driving the subsequent pulse detection circuitry and data restoration stages in the Manchester decoder.

5.0 MANCHESTER ELECTRONICS

The Manchester encoder and decoder electronics has been designed, built, and installed into the demonstration system. The details of its function and design are described in this section.

The 1300-nm downlink carries a Manchester-encoded 19.2-Kbaud signal. This signal is decoded by a Manchester decoding circuit. Of course, serial transmission of data is necessary since only one fiber is used in the communications system. Even if many fibers could be used in the cable, serial communication would still likely be preferred because long parallel data links are more costly and introduce skew between adjacent bits when the link is long. The main objectives of a communication link are data integrity and high data rate and these are easily achieved using a serial architecture.

5.1 BACKGROUND

Two of the most popular coding schemes used in digital fiber-optic communications are Nonreturn to Zero (NRZ) and Return to Zero (RZ), represented by classes of binary biphasic codes such as the Manchester code. In general, an NRZ code changes state when the data either change from logic 1 to logic 0 or from logic 0 to logic 1. The Manchester waveform changes state in the middle of a clock pulse, which results in a series of state transitions at the clock frequency whether the data changes or not (Sander, 1982a and b). A high level in the first half of the clock period represents a logical 1, and a high level in the second half of the clock period represents a logical 0. This midperiod transition results in the data and the clock being combined into one composite signal (in a code, this feature is known as being "self-clocking"). The Manchester code also results in the signal having a constant average value, which means that it can be transmitted without sending a DC component. The NRZ format, on the other hand, changes state only when a bit changes state and even then only at the end of a clock pulse. This results in fewer transitions per second than a biphasic code, which in commercial applications is a great advantage since a fiber is simply thought of as a conduit for a given number of telephone calls (more is better, without great regard for increased electronics complexity). The greatest disadvantage of the NRZ format is that the clock information can be lost if a long run of 1s or 0s occurs in the data stream unless measures are taken to prevent this occurrence; therefore, synchronization becomes an issue (Morris, 1983). The Manchester code, on the other hand, has many advantages: it is self-clocking, incorporates inherent error detection, and allows alternating current (AC) coupling of the waveform. That extra bandwidth is required for transmission is the main disadvantage of the Manchester code; it requires *twice* the bandwidth as the NRZ code for the *same* baud rate.

The command-control downlink data rate of 19,200 baud is miniscule compared to the information-carrying capacity of a dispersion-shifted single-mode fiber operating at 1300 nm, making the only disadvantage of Manchester encoding insignificant. Therefore, Manchester code was chosen to transmit the command-control signal.

5.2 MANCHESTER ENCODER

The function of the Manchester encoder is to encode the command-control downlink data into sequential blocks of data that can be transmitted efficiently over the fiber-optic cable. Figures 5 and 6 show the block diagram and electronic schematic for the encoder, respectively. The information is clocked out to the 1300-nm laser transmitter. Data from the computer terminal are input asynchronously to the encoder circuitry at the data rate of 19.2 Kbrs. The main function of the Universal Asynchronous Receiver Transmitter (UART) is to take in serial data and serially shift that data out in

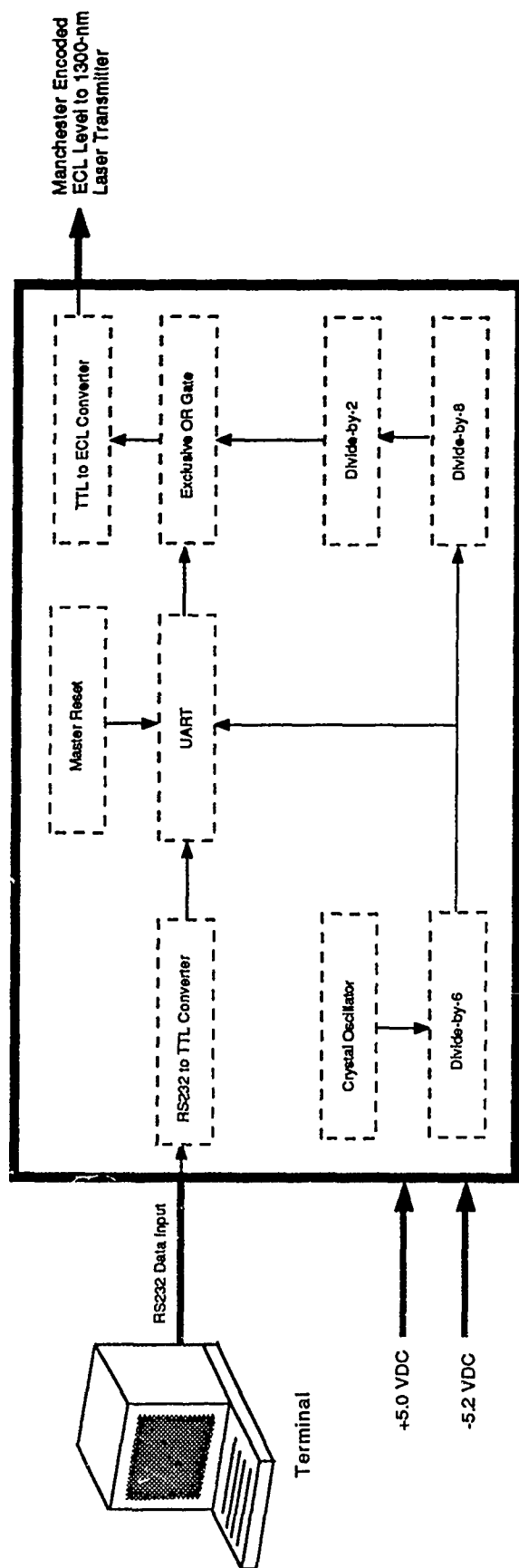


Figure 5. Block diagram of Manchester encoder.

the form of start bits, data bits, and stop bits. It is then put through an exclusive OR with a stable 19.2-KHz clock generated by a crystal, the output being the Manchester-encoded data. The 1300-nm laser transmitter requires an ECL signal, therefore the data are transformed from TTL to ECL with a converter. A TTL-level laser transmitter bias alarm provides overbias information for a laser health indicator and can be monitored.

5.3 MANCHESTER DECODER

The purpose of the Manchester decoder is to retrieve the clock and the data and to convert the data to an RS-232 level. Figures 7 and 8 illustrate the decoder block diagram and electronic schematic, respectively. From the optical receiver, the Manchester-encoded data are AC-coupled to remove any DC component. The comparator takes a relatively small signal and outputs a TTL-level signal. A phase lock loop is then used to extract the clock from the Manchester code. With the extracted clock, data are sequentially clocked out of a "D" flip flop. After converting to RS-232, the data are sent to the receiving terminal, which completes the link.

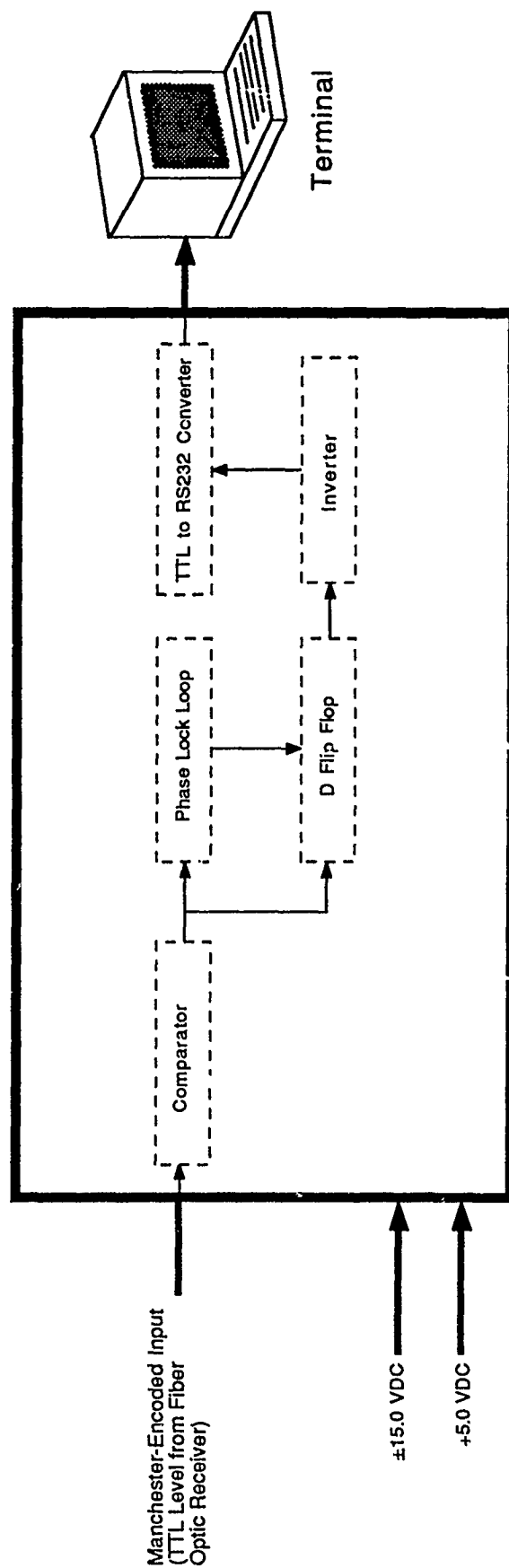


Figure 7. Block diagram of Manchester decoder.

5.0 PFM HARDWARE ALTERATIONS

6.1 INTRODUCTION

The original PFM encoder/decoder system was optimized such that National Association of Broadcasting (NAB) Standard ($S/N > 55$ dB) video signal-to-noise ratio (S/N) specifications were achieved for optical signal levels just over threshold. This is conservative for most applications; in fact, for all but studio monitoring applications, $S/N > 40$ dB is perceived by most users as being "noiseless." Advantage can be taken of this fact to lower the threshold of the PFM system significantly at the expense of the S/N near threshold. Changes in the PFM transmitter hardware and receiver bandwidth will result in improved optical sensitivity if the minimum acceptable S/N near threshold is reduced somewhat from its present value.

It is well known that lower receiver bandwidth provides higher optical sensitivity. This is because the higher value of transimpedance resistor in a lower bandwidth PIN-FET produces less Johnson noise. Additionally, some of the remaining noise energy is filtered out at higher frequencies by virtue of the reduced cutoff frequency of the lowpass filter following the preamplifier. Typically, a factor of 2 reduction in detector bandwidth results in at least a 3-dB improvement in receiver sensitivity, although the lower predetection bandwidth results in less spread-spectrum processing gain, lowering S/N correspondingly. However, by judicious choice of parameters the S/N can still be made greater than 40 dB when the system is above threshold and, therefore, the noise will not cause the end user a problem.

The bandwidth of the original PIN-FET receiver was 50 MHz. For a threshold $C/N = 16$ dB this gives a calculated S/N of 52 dB at the output of the PFM decoder at threshold. If the receiver bandwidth is reduced to roughly 32 MHz, the S/N falls to 48 dB near threshold. An S/N greater than 40 dB is considered adequate and fully usable for video reception, so $S/N = 48$ dB is acceptable. The reduction in receiver bandwidth from 50 to 32 MHz will result in approximately a 2-dB improvement in the optical sensitivity, which is significant. This estimate is based on typical PIN-FET receiver sensitivities at those two bandwidths. Refer to the next section for the relationship between sensitivity and bandwidth.

6.2 RECEIVER OPERATING CHARACTERISTICS

The following figures show the measured S/N versus C/N for an actual PFM modulator/demodulator pair when the transmitted pulse consists of an impulse (resulting in the receiver generating an impulse response corresponding to its frequency response). Such a relationship between S/N and C/N is called a Receiver Operating Characteristics (ROC). Unlike theoretical analyses, such a measured performance relationship requires no assumptions based upon approximations and includes the additional noise introduced by the actual signal-processing hardware and the video amplifier chain. It is noted that, in absolute terms, reducing the predetection bandwidth causes the postdetection S/N to decrease correspondingly due to the reduction in spread-spectrum gain. However, the C/N required to achieve the operating threshold does *not* change, confirming that use of a lower bandwidth PIN-FET will indeed improve the optical sensitivity of the receiver at threshold. An output $S/N > 40$ dB is easily achieved in either case.

Figures 9 and 10 show the measured ROCs for 66- and 20-MHz decoders, respectively. These bandwidth values bracket the region of operation of the PFM system. The plots show S/N versus C/N over increasing values of preemphasis. The results of the measurements plotted in figures 9 and 10 are used to generate figure 11. Figure 11 plots the measured S/N as a function of incident optical power

level for 20- and 66-MHz decoders. To achieve this plot, the measured C/N values at various S/N values are taken from the middle preemphasis curve of figures 9 and 10. Next, the peak incident power is estimated by inserting the bandwidth and C/N values into a curve-fit equation, equation 6. This equation fits the typical peak sensitivities of the five leading PIN-FET manufacturers over a bandwidth range of 10 to 200 MHz. For reference, this equation is given below. The typical peak sensitivity, P_{rx} , for a PIN-FET is estimated as

$$P_{rx} = -(21.5 - C/N)/2 - 61.82 + 10.848 \log_{10}(1.4 BW_{RF}) \quad (\text{dBm}) \quad (6)$$

where C/N is the carrier-to-noise ratio in dB
and BW_{RF} is the RF bandwidth in MHz.

As seen in figure 11, for a $S/N = 40$ dB, the required incident peak power at the detector is between -42.5 dBm (for 66 MHz) and -47.5 dBm (for 20 MHz). The original system employs a 50-MHz receiver with a measured peak sensitivity of -45.75 dBm at a $C/N = 16$ dB. The estimated sensitivity of -44.6 dBm obtained from equation 6 compares favorably to this value.

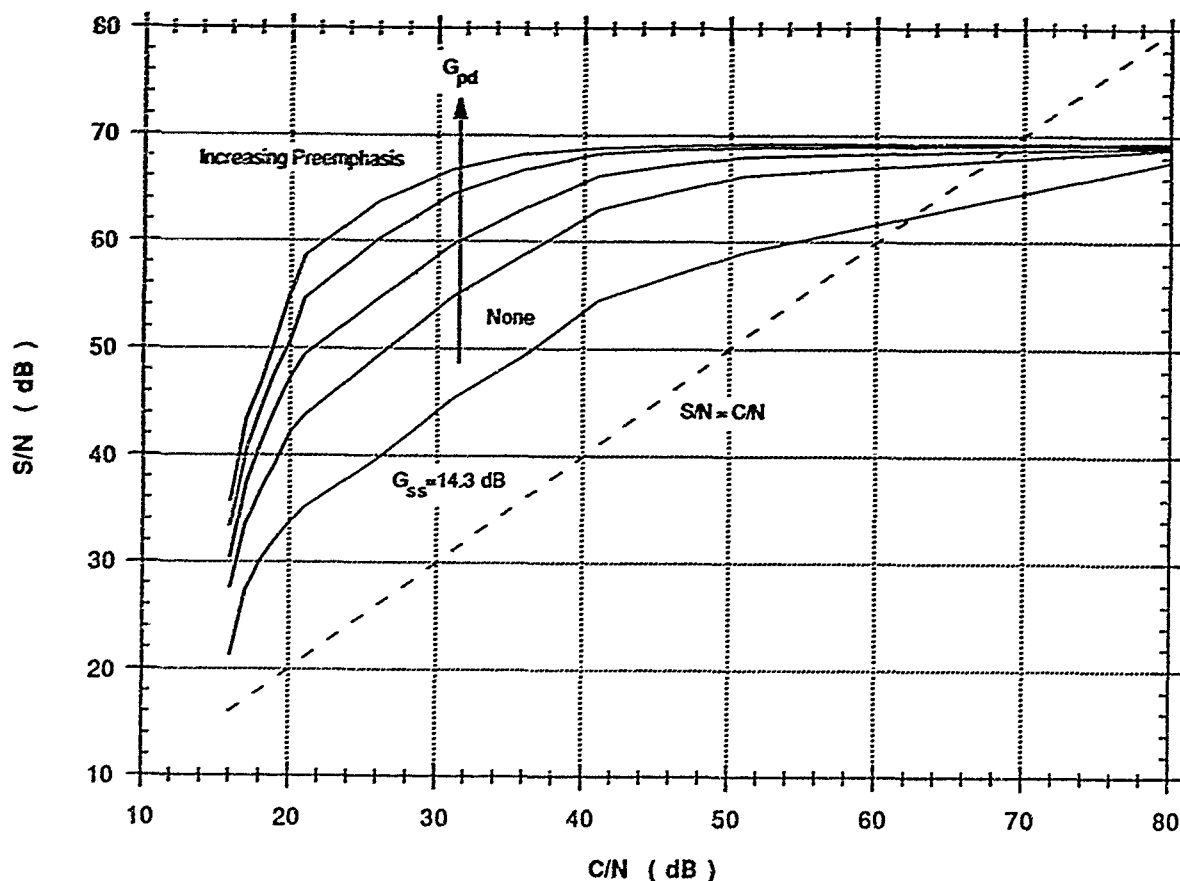


Figure 9. Receiver operating curves, S/N versus C/N, for 66-MHz PFM decoder.

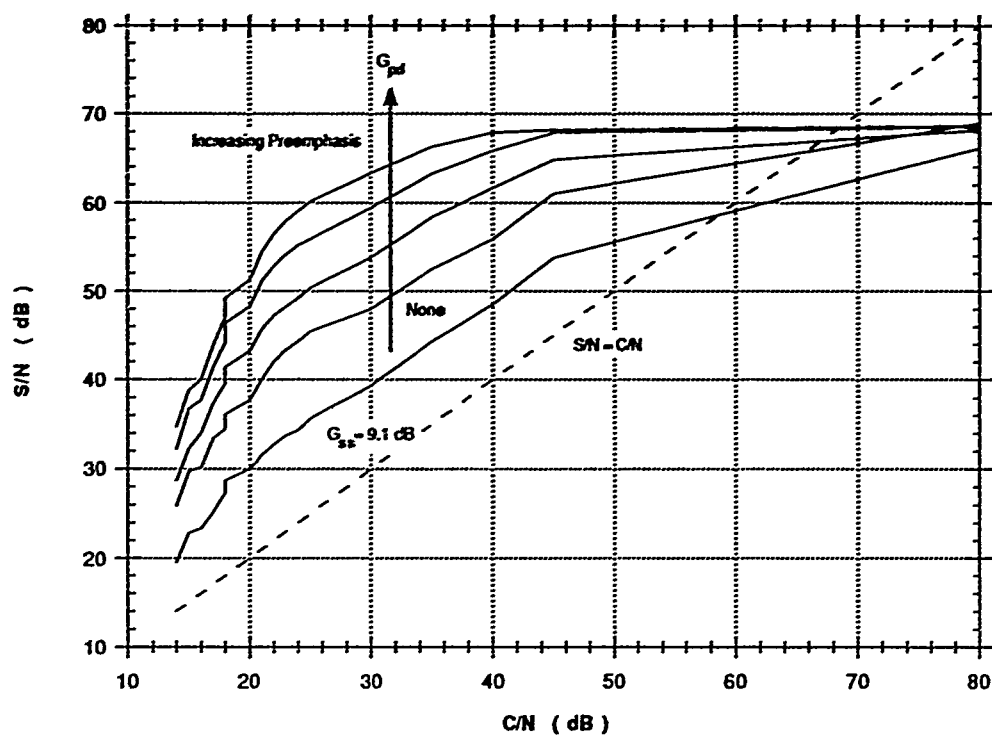


Figure 10. Receiver operating curves, S/N versus C/N, for 20-MHz PFM decoder.

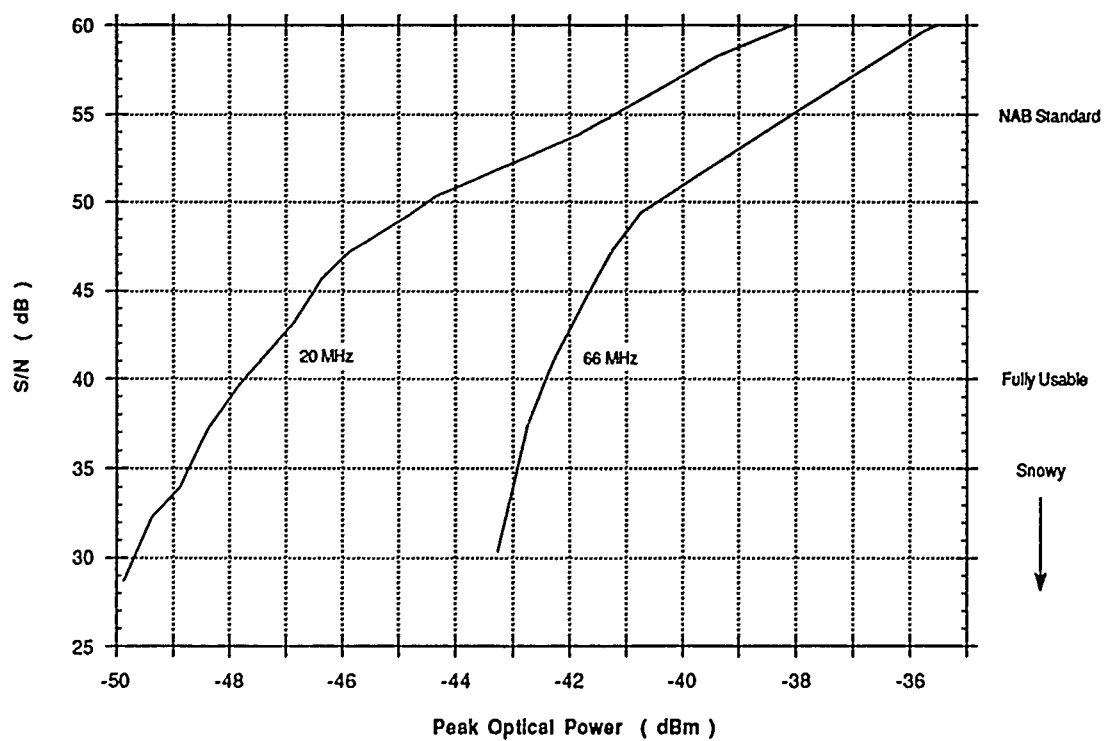


Figure 11. Comparison of PFM decoder threshold characteristics, 20- and 66-MHz RF bandwidth.

6.3 PULSE WIDTH REQUIREMENTS

The duration of the transmitted PFM pulse, which marks the time interval corresponding to the analog video level, must satisfy three simultaneous conditions:

A. The pulse must be long enough to permit the signal to achieve full amplitude given the system risetime (system bandwidth).

$$W > 0.5/BW \quad (7)$$

where W = transmitted pulse width
and BW = system risetime (transmitter + fiber + receiver).

For maximum sensitivity, the system should operate on or near this line, as it defines the optimum C/N possible as well.

B. The pulse must not be so long that the duty factor of the PFM signal exceeds 50% for the highest PFM pulse repetition frequency, or the signal inverts itself for large deviations.

$$f_{\max} = f_c + \Delta f \quad (8)$$

where f_{\max} = highest PFM pulse repetition frequency
 f_c = carrier frequency
and Δf = deviation.

$$T_{\text{FWHM}} = 0.32/BW$$

where T_{FWHM} = pulse width at 50% slicing level. This is based upon the impulse response of a linear phase filter.

$$[1/(f_c + \Delta f)]^2 > 2[(0.32/BW)^2 + W^2] \quad (9)$$

$$W^2 < 0.5[1/(f_c + \Delta f)]^2 - (0.32/BW)^2 \quad (10)$$

C. The pulse must not be so long as to prevent it from approaching the baseline between pulses at the maximum pulse repetition frequency or intersymbol interference and AGC errors will result. Since *full* pulse widths are of concern, the times are added *algebraically* to simulate the effect of the convolution that actually takes place. This is a good approximation for a nearly rectangular optical pulse convolving itself with the impulse response of the receiver, which is optimally a raised cosine window.

$$T_{\text{SETTLING}} = 1/BW \quad (11)$$

where T_{SETTLING} = Full width of pulse required for it to settle to within a small error from the baseline. Clearly the settling time can be larger if significant ringing is present, hence the requirement for a linear phase response for the system.

$$W < 1/(f_c + \Delta f) - 1/BW \quad (12)$$

These relationships all assume a Gaussian-shaped pulse. The three relationships are plotted in figure 12, clearly showing an allowed region for the pulse width. As the bandwidth of the system is made smaller (less than about 40 MHz), this effect must be considered. It appears that to use a system bandwidth of 32 MHz to increase the receiver sensitivity, the pulse width must be equal to 16 nsec.

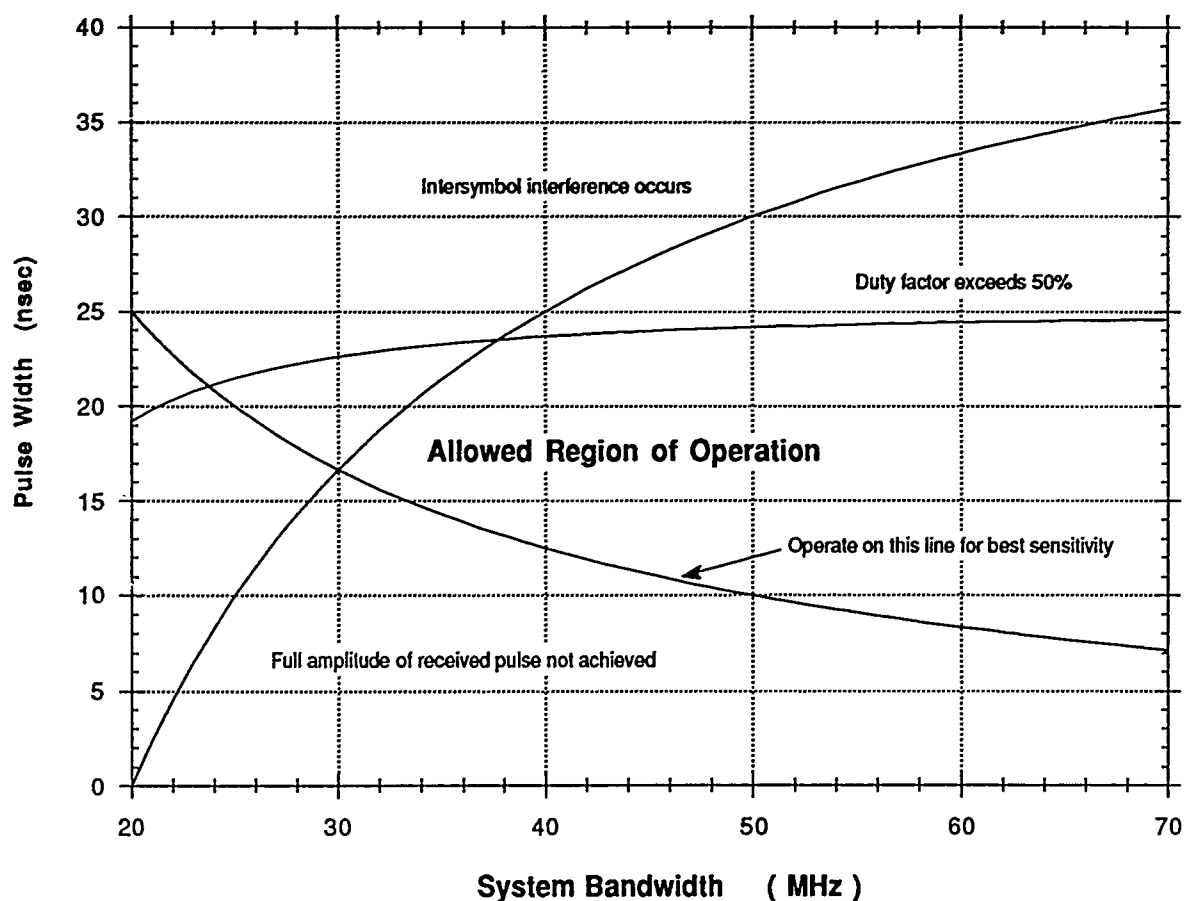


Figure 12. Determination of PFM pulse width.

6.4 HARDWARE IMPLEMENTATION AND RESULTS

To achieve the sensitivity improvement, two main changes to the PFM encoder and decoder were implemented. The original 50-MHz receiver bandwidth of the photodetector is reduced, increasing its sensitivity by reducing the thermal noise from its preamplifier. Based on bandwidth considerations for PFM, the transmitted pulse width must be small compared to the period of the carrier plus the maximum signal deviation (Cowen, 1979). However, to compensate for the reduced bandwidth at the receiver, the transmitted pulse width must be broadened or the pulse will not achieve full amplitude within the receiver risetime. Originally the pulse width was 12 ns, permitting full pulse amplitude to be achieved with a system bandwidth of 50 MHz. For a predetection bandwidth equal to 32 MHz, the pulse width was increased to 16 ns. Pulse widths greater than 16 ns must be avoided, as longer pulses lead to intersymbol interference near maximum signal deviation, causing signal distortion.

As a point of reference, the PFM block diagrams are given. Figure 13 is the PFM encoder, and figure 14 is the PFM decoder. A pulse width stretcher circuit was placed between the output of the PFM encoder and the laser transmitter. The circuit stretches the original 12-ns ECL input pulse width into a 16-ns ECL output pulse.

The net improvement in the optical margin was measured and compared with the original PIN-FET receiver bandwidth and transmitted pulse width. The results indeed show an improved margin. The net gain in sensitivity is 2 dB. This result agrees with the estimated gain.

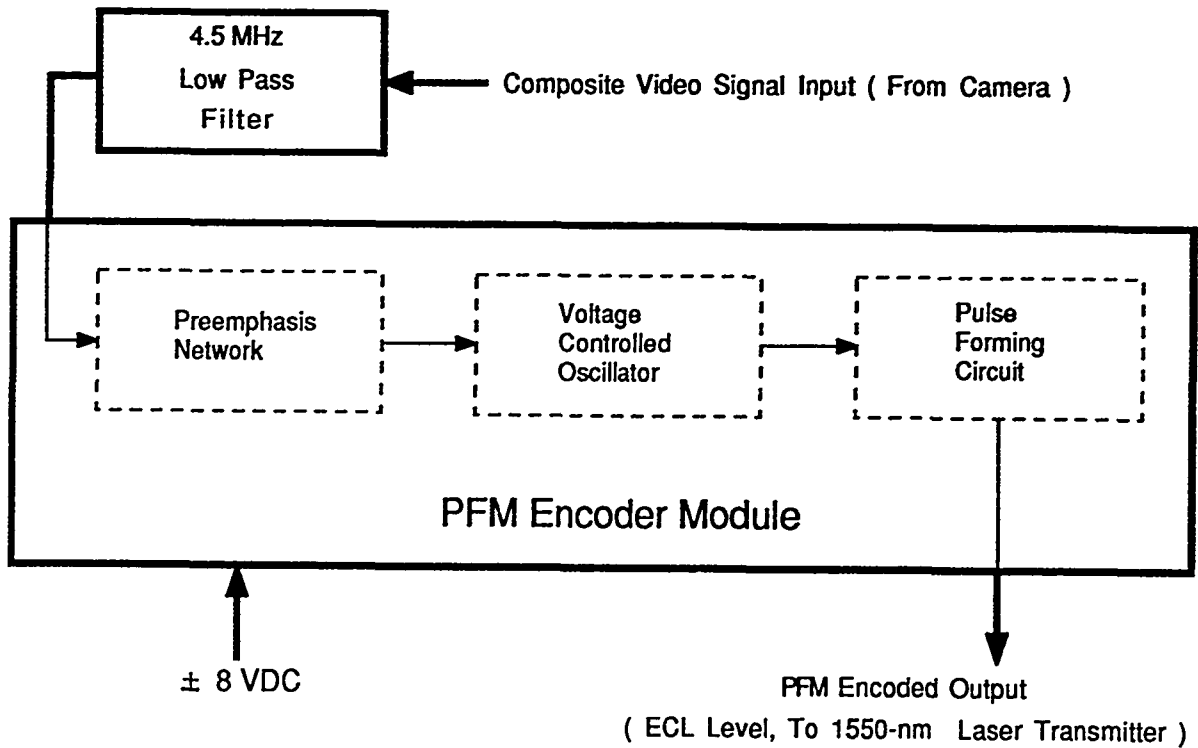


Figure 13. Block diagram of PFM encoder.

The measured performance data for the new PIN-FET are given in table 3.

Table 3. Measured performance data for new PIN-FET.

Manufacturer: PCO, Inc.		
Model: RTZ-45-32 MHz-050		
Bandwidth	55.8	MHz
Responsivity at 1.3 μm	0.82	A/W
Noise equivalent input power	2.6	nW
Transimpedance	99	K Ω
PIN leakage current at -5 Volts	2.1	nA
Average sensitivity at 45 Mbit/s	-48.1	dBm
Peak sensitivity at C/N = 16 dB	-47.8	dBm
Receiver gain	81.2	mV/ μW

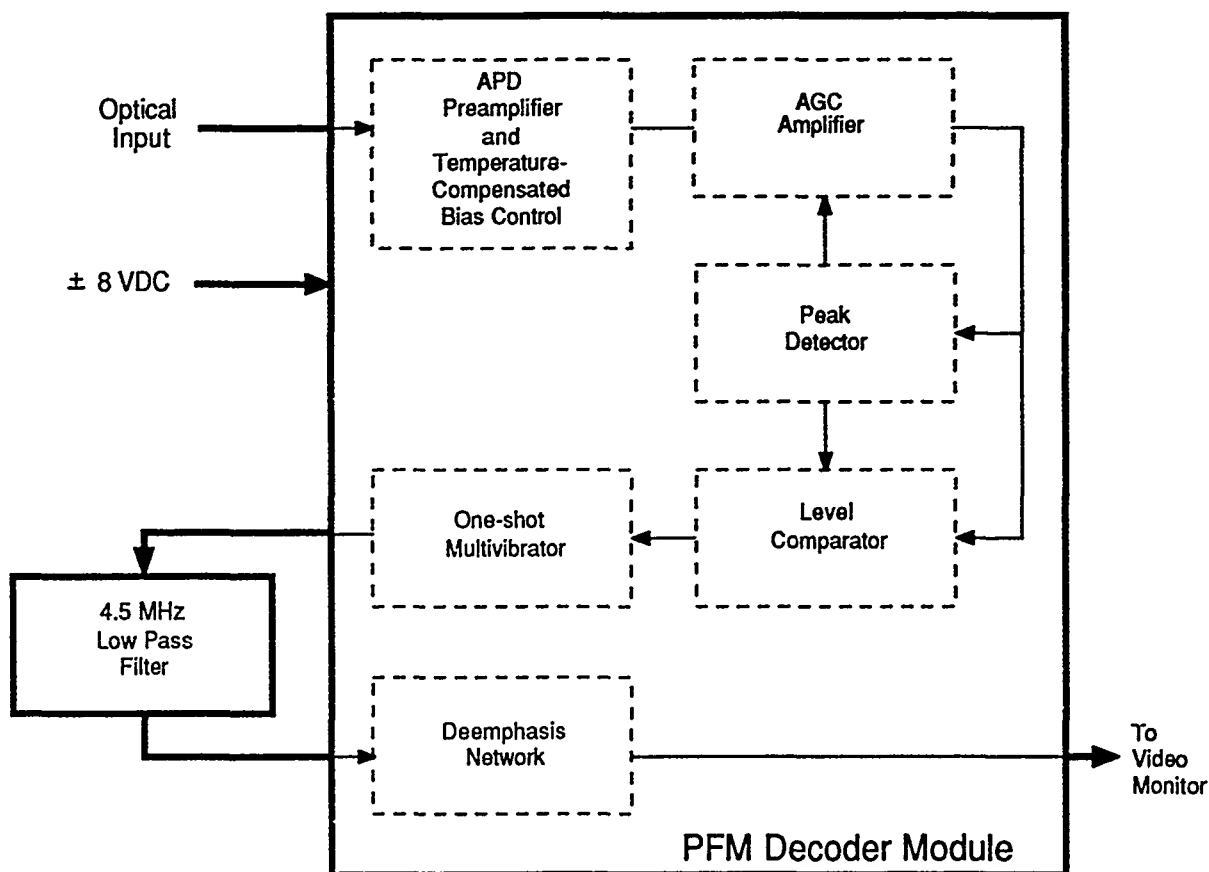


Figure 14. Block diagram of PFM decoder.

7.0 AVALANCHE PHOTODIODE (APD) RECEIVER

7.1 INTRODUCTION

The PIN-FET detector module, which consists of a unity-gain PIN photodiode coupled to a low-noise GaAs FET preamplifier, has become the industry standard as an opto-electronic detector in fiber-optic transmission systems due to its good overall performance and application simplicity. Other types of photodetectors are capable of higher signal sensitivities, however, but their greater complexity and cost have tended to favor adoption of the PIN-FET commercially. In a high-performance repeaterless data link, sensitivity is critical since each additional decibel translates into 4 to 5 kilometers of added transmission distance, making cost and complexity less of a driving concern than for typical commercial systems. An APD is capable of detecting considerably weaker optical signals than the PIN-FET, which is employed in the existing demonstration system due to its signal multiplication

mechanism with only a modest increase in cost and complexity. For the same optical input level, a higher signal current output level is generated by an APD than for a PIN photodiode. So long as a net increase in signal current accrues compared with noise current, a net sensitivity improvement for the receiver results. This section discusses the theory, design, production, and testing of an APD receiver suitable for replacing the PIN-FET in the existing NOSC fiber-optic demonstration system.

7.2 THEORETICAL SENSITIVITY ANALYSES

The 1550-nm receiver sensitivity has been improved by replacing the original PIN-FET with an APD receiver. It is recognized that an APD, with internal gain, can offer improved sensitivity, at optimum conditions of gain, over a PIN-FET. Several factors affect the overall improvement in sensitivity. Prior to designing and constructing an APD receiver for the PFM decoder, an in-depth theoretical analysis was performed. This was done to predict the magnitude of sensitivity achievable with an APD. The APD bandwidth was set to 50 MHz to compare to the original PIN-FET bandwidth. It was felt that gains of 3 dB or better would warrant the integration of an APD receiver into the 1550-nm channel. The net extension in standoff range is worth the additional complexity required for the APD receiver.

This section details the theoretical analyses. Several approaches are used to predict the optimum APD sensitivity based on both typical and measured APD parameter values. First, the C/N equations used for the analyses are discussed. Then various solutions for sensitivity are found and compared to the PIN-FET performance.

7.2.1 Noise Equations

Sensitivity, most often given in units of decibels relative to 1 milliwatt (dBm), is a measure of a receiver's ability to detect low levels of optical signal power in the presence of noise. For digital systems, the sensitivity is most commonly specified as the incident optical power required at the receiver to maintain a bit error rate (BER) of 10^{-9} or better. For a thermal-noise-limited receiver, a reasonable assumption for fiber optics where light levels below -40 dBm are common, a BER of 10^{-9} corresponds to a C/N of 21.5 dB, electrical. The C/N is defined as the ratio of the peak electrical signal power to the rms noise power. For analog systems, such as PFM, sensitivity is specified for a C/N at threshold. For the duplex demonstration system, the threshold C/N is set at 16 dB. This value is used in the analysis to predict the required input power or sensitivity at the APD receiver. The derived power is compared directly to the PIN-FET performance.

From the definition of C/N, an equation is written

$$C/N = i_s^2 / \langle i_{n_{APD}} \rangle^2 + \langle i_{n_{amp}} \rangle^2 \quad (13)$$

The term in the numerator is the square of the peak signal current generated by the APD so

$$i_s = \rho MP \quad (14)$$

where ρ is the APD responsivity at unity gain in amps/watts (A/W), which is found from the detector's quantum efficiency and signal wavelength using the equation

$$\rho = \eta e \lambda / hc \quad (15)$$

where η is the detector quantum efficiency
 e is the electronic charge

λ is the incident-signal central wavelength
 h is Planck's constant
and c is the speed of light in a vacuum.
 M is the internal gain of the APD
and P is the peak signal power incident on the detector surface.

The terms in the denominator of equation 13 represent the noise sources at the receiver. Noise generated by the transmitter is negligible and neglected. The left term in the denominator is the mean-square shot-noise current from the APD generated from the incident optical signal and from multiplied bulk current and unmultiplied leakage current. The right term is the mean-square shot- and thermal-noise current from the preamplifier's bias and feedback resistors. For the preliminary analysis, the preamplifier noise was derived from a Texas Instruments (TI) data sheet for a low-noise high-speed transimpedance amplifier. The APD shot-noise term is expanded based on Gaussian statistical noise equations as follows:

$$\langle i_{n_{APD}} \rangle^2 = 2eB_n(((\rho P/2) + I_{bulk})M^2F(M) + I_{surf}) \quad (16)$$

where e is the electronic charge, 1.602×10^{-19} (A·s)
 B_n is the receiver predetection bandwidth (Hz)
 I_{bulk} is the reverse bulk current of the APD (A)
 I_{surf} is the surface leakage current of the APD (A)
 $F(M)$ is the excess noise factor for average gain M of the APD

and ρ , M , and P are the responsivity, gain, and incident peak power, respectively, as defined for the signal current in equation 14.

Further expansion of $F(M)$ gives

$$F(M) = k_{eff} M + (1 - k_{eff})(2 - 1/M) = M^x \quad (17)$$

where k_{eff} is the electron/hole ionization coefficients ratio
and x is the excess noise coefficient.

In addition to gain in the APD, excess noise is present. Excess noise is due to the randomness of the avalanche gain mechanism in the APD. The excess noise is related to the ionization coefficients ratio, k_{eff} . A typical value for k_{eff} for an indium gallium arsenide (InGaAs) APD is 0.5. Note that the bulk current is multiplied by the avalanche gain while the surface leakage current is unmultiplied.

Inserting the input signal term, equation 14, and the APD, equation 16, and preamplifier noise terms into equation 13 gives the general C/N equation:

$$C/N = (\rho MP)^2 / 2eB_n(((\rho P/2) + I_{bulk})M^2F(M) + I_{surf}) + \langle i_{n_{amp}} \rangle^2 \quad (18)$$

This equation is used for both PIN and APD-type receivers. For PIN receivers M and $F(M)$ are equal to unity.

From the general C/N equation, equation 18, it is seen that an optimum gain M for the APD exists. At low levels of gain, the signal power increases faster than the noise power and the preamplifier noise dominates. Above optimum gain the excess noise causes the sum of the APD shot noise and preamplifier noise to increase faster than the signal power. The optimum gain occurs approximately where the APD noise just equals the preamplifier noise. The exact optimum can be found by taking the derivative of equation 18 with respect to M and setting it equal to zero. In practice this optimum

is found by increasing M until the noise begins to degrade the C/N. The gain of an APD is sensitive to temperature fluctuations. The APD receiver uses a circuit that maintains a constant gain for the APD over a wide temperature range once the optimum gain is set.

7.2.2 Sensitivity Predictions

The best sensitivity is at optimum gain. To find this sensitivity, peak power P is solved for in equation 18, letting M vary. To perform this calculation all other variables had to be quantified. Different approaches are taken to arrive at a theoretical APD sensitivity. The first approach uses typical values of a transimpedance amplifier and an InGaAs APD provided by the manufacturer. The APD sensitivity is compared to the original 50-MHz PIN-FET. From a TI data sheet for a 50-MHz transimpedance amplifier, TIEF151, the amplifier noise-current spectral density is typically 4.5 pA/√Hz. So at 50 MHz

$$\langle i_{n_{amp}} \rangle^2 = 1.01 \times 10^{-15} \text{ A}^2.$$

Other variables were obtained from an APD manufacturer's data sheet. For the RCA* C30645EQC, the following *typical* values are taken:

$$\begin{aligned} \eta &= 0.70 \text{ at } \lambda = 1550 \text{ nm } (\rho = 0.873 \text{ A/W}) \\ I_{bulk} &= 5 \text{ nA} \\ I_{surf} &= 1 \text{ nA} \\ k_{eff} &= 0.5 \end{aligned}$$

Also B_n was set at 50 MHz to match the bandwidth of the TI preamplifier and the original PIN-FET. C/N is set to 16 dB for PFM threshold (Cowen, 1979). Of course the C/N is converted to a unitless ratio of 39.8 when used in the solution of P .

Figure 15 illustrates the results of the solution for sensitivity, P , for two different values of pre-amplifier noise. Plotted is peak sensitivity in dBm as a function of gain M . The upper curve is for the TIEF151 preamplifier with a noise-current spectral density of 4.5 pA/√Hz. The initial results, using the TIEF151, were not encouraging. The PIN-FET sensitivity is shown for comparison. Note that the PIN-FET sensitivity is shown as a single data point at a gain of 1. Using the typical values for the APD and the TI preamplifier, the sensitivity for a APD receiver is about -45.4 dBm at an optimum gain of about 25 compared to -45.75 dBm for the PIN-FET receiver. The PIN-FET is 0.35 dB more sensitive. The relative flatness of the APD sensitivity as a function of gain is one indication that the preamplifier noise is too large. For the second calculation, the sensitivity was found for an APD receiver using a preamplifier with a noise-current spectral density of 2.0 pA/√Hz. This is shown as the lower curve in figure 15. For this configuration, the APD sensitivity is predicted as -46.75 dBm or 1 dB better than the PIN-FET. Note how reducing the preamplifier noise gives a more defined optimum gain around a value of 17 for the lower curve.

* RCA Inc., Electro-Optics, 773 Donegall Business Center, P. O. Box 540, Mount Joy, PA 17552-0540, (717) 653-9122

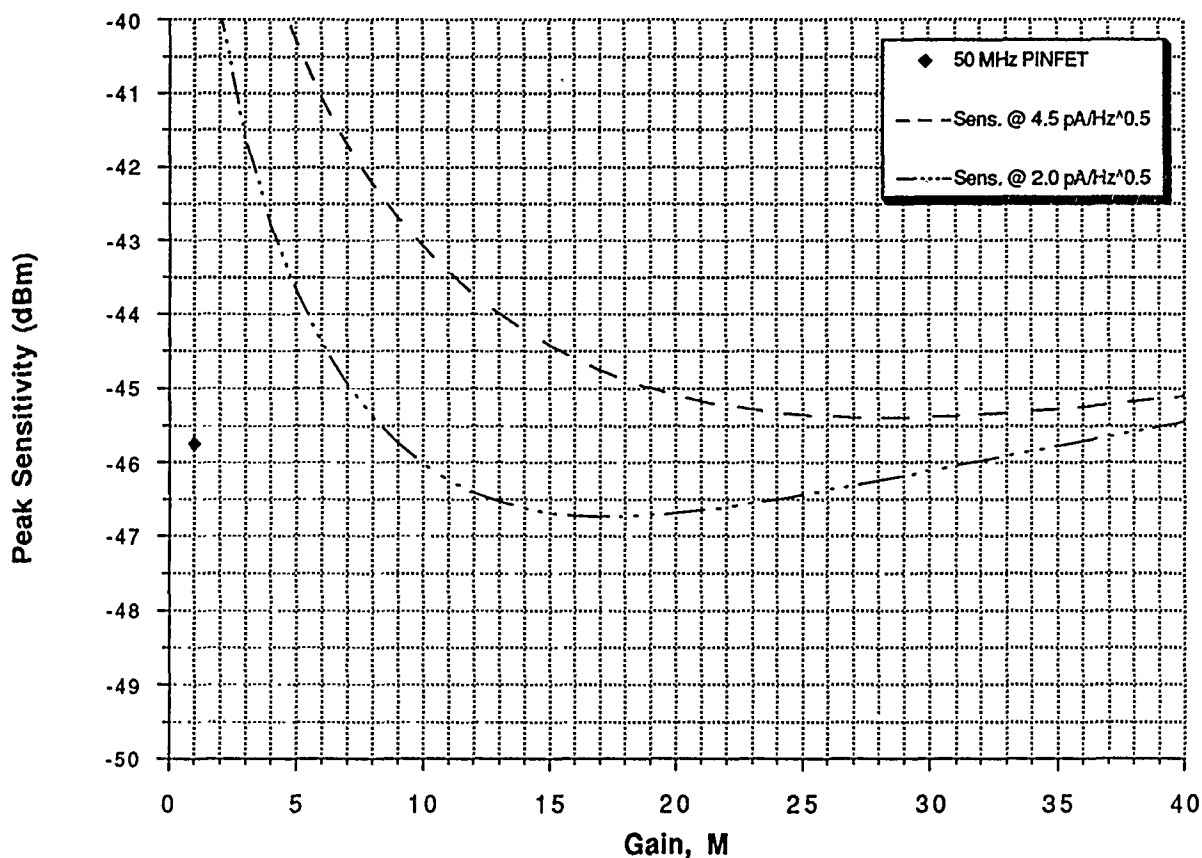


Figure 15. Peak sensitivity versus APD gain at various pre-amp noise values. ($C/N = 16$ dB, 50 MHz).

The general C/N equation, equation 18, has limitations. Difficulty arises in accurately predicting the APD signal and noise currents. Gain is difficult to measure directly. It is also not usually possible to determine the bulk and surface currents unambiguously. Instead, the dark current as a function of reverse bias voltage is usually measured first. Next the total current, photocurrent plus dark current, is measured as a function of reverse voltage. The approximate gain as a function of reverse voltage is then derived from these two measurements.

For figure 15 the bulk current is set for the APD at unity gain, and then the equation works to magnify this current as the gain increases. More accurate estimates for dark current noise as a function of gain were analyzed. APD manufacturers often supply curves of gain and dark current versus reverse bias voltage with the data sheet. RCA provided these curves for the RCA APD model C30645EQC. The curves were then translated into computer files and were plotted. Figure 16 shows the measured dark current and gain versus reverse bias or operating voltage. Figure 17 is a plot of dark current versus gain. It is derived from the data in figure 16 over a range of gain between 5 and 25. Figure 18 is a plot of the measured noise-current spectral density versus gain taken from an RCA APD data sheet. As shown in figures 17 and 18, curve-fit equations were generated from the data. These equations are then used in the general C/N equation to more accurately predict the APD sensitivity.

As expected, the results of the more precise noise analyses show that the receiver sensitivity is limited mostly by the preamplifier noise compared to the APD shot noise for gains less than and equal to the optimum. No change in sensitivity is observed from the more precise APD noise modeling. Figure 19 illustrates the normalized signal and noise powers at the APD receiver at threshold C/N for a $2.0\text{-pA}/\sqrt{\text{Hz}}$ preamplifier. As is seen, the preamplifier noise dominates for APD gains up to roughly 13. The carrier power increases as the square of the APD gain. The APD shot noise increases faster since excess noise also contributes. Of course the preamplifier noise is independent of the APD gain. This plot illustrates the point where an optimum gain is achieved. Beyond the optimum, the C/N is degraded by further increases in APD shot noise.

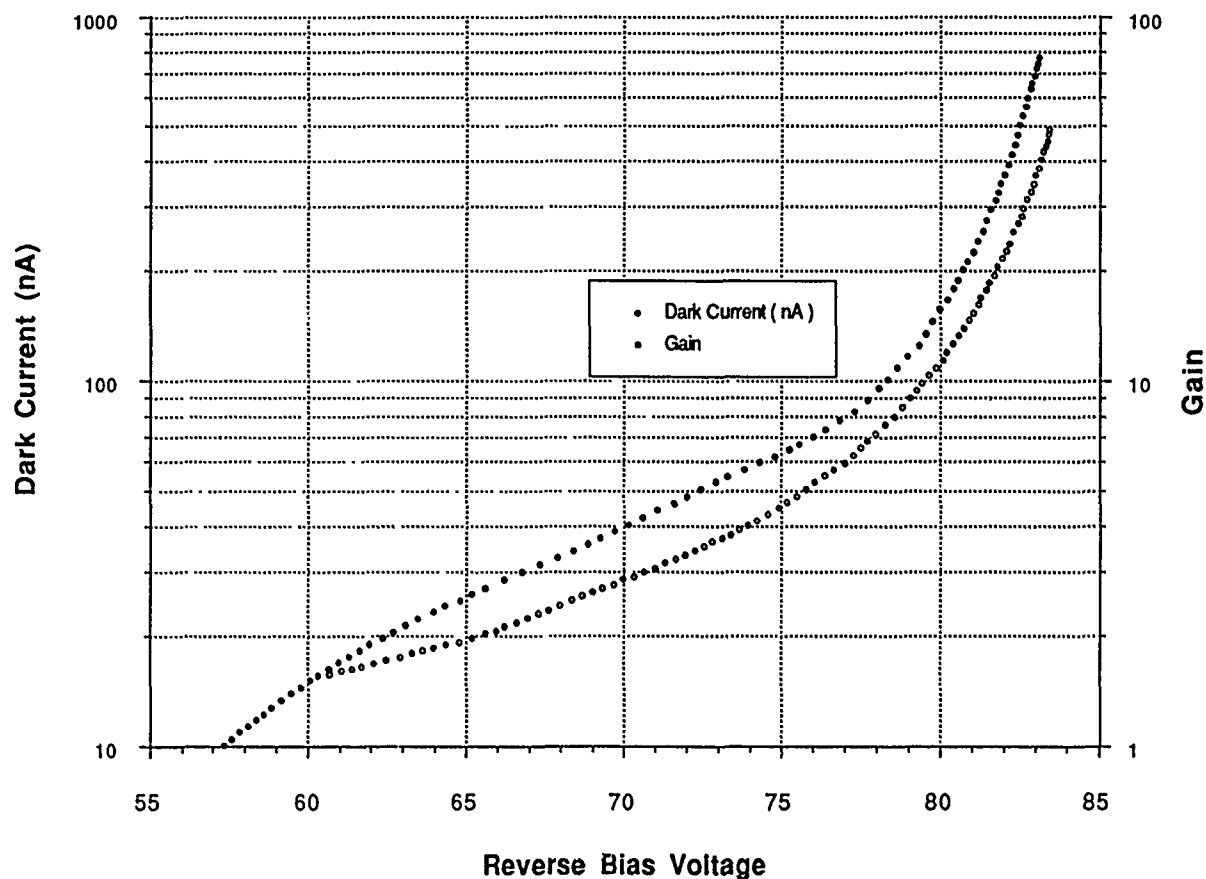


Figure 16. Dark current and gain versus bias voltage for RCA APD.

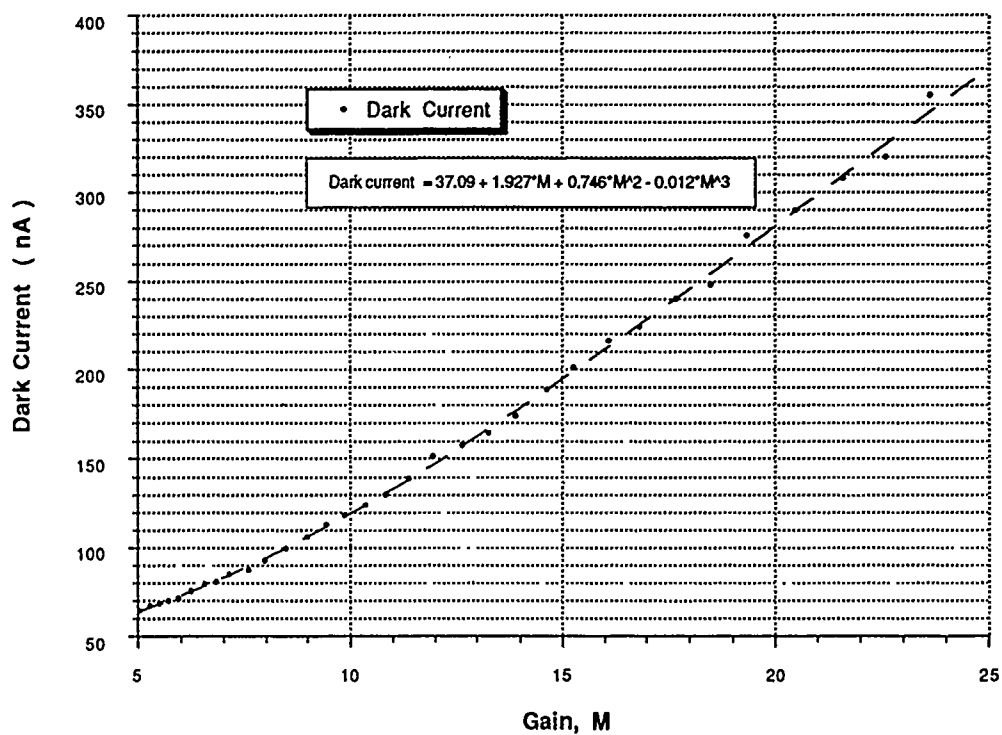


Figure 17. Dark current versus gain for RCA APD.

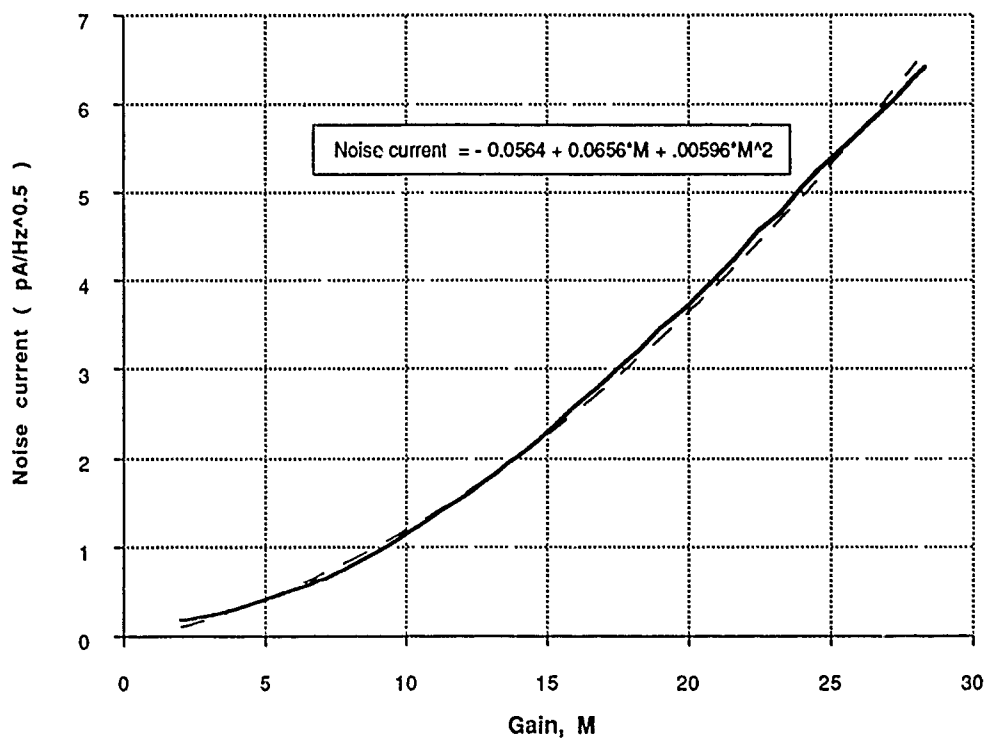


Figure 18. Noise current versus gain for RCA APD.

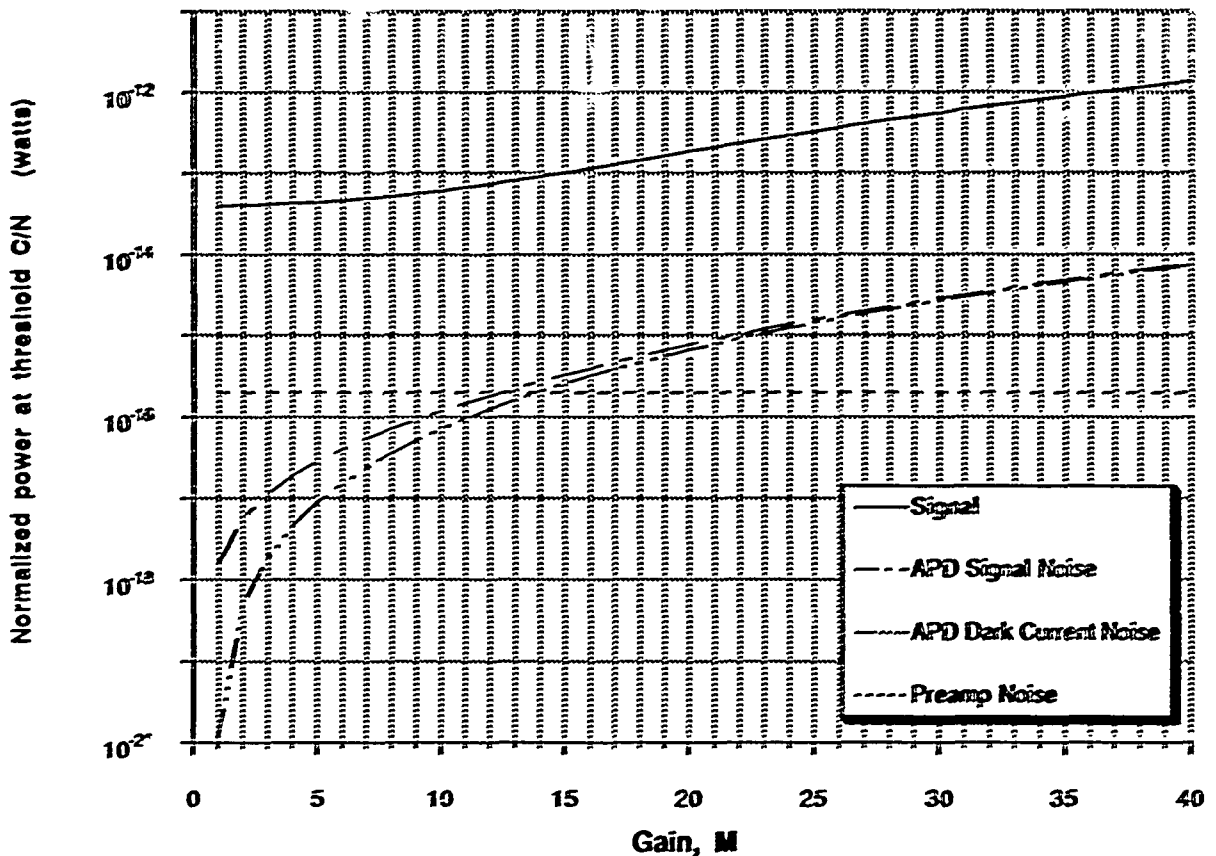


Figure 19. Normalized carrier and noise powers at the APD receiver.

7.2.3 Summary of Theoretical Analyses

While the analyses reveal only slight improvement, 1 dB, using a 50-MHz APD receiver it was decided to design and build an APD receiver in an attempt to outperform the existing PIN-FET. The bandwidth goal was 32 MHz. It is apparent from the plots in figure 15 that a low-noise preamplifier is critical to the success of the receiver design. The APD manufacturer originally specified a typical noise current of 2.0 pA/ $\sqrt{\text{Hz}}$ from the APD at optimum gain. Therefore, it is necessary to build a preamplifier with a noise level as close to or less than this value as possible.

7.3 APD RECEIVER DESIGN AND PRODUCTION

7.3.1 Introduction

This section discusses the design and production of the APD receiver. The purpose of changing the receiver design from a P-I-N photodiode/FET preamplifier (PIN-FET) receiver to an APD receiver is to increase the repeaterless standoff range of the 1550-nm channel.

7.3.2 Comparison of Performance Between PIN-FET and APD

A PIN photodiode is, at best, a unity-gain optical-to-electrical converter, that is, for each incident photon received on the surface of the device, at most one electron is generated at its output.

In general, the "photon-to-electron conversion ratios" (quantum efficiency) of a PIN photodiode is less than unity: typically on the order of 80 to 90% for a well-designed device. This means that very small signal currents appear at the output of the device for weak optical input signals; therefore, the photodiode's preamplifier noise factor is critical in establishing the low-noise floor required for a sensitive receiver. To achieve high-optical sensitivity, two design steps are typically taken: a low-noise, high gain-bandwidth product semiconductor device (typically a GaAs FET) is used as the first stage of the preamplifier following the photodiode, and the photodiode and preamplifier are integrated onto the same substrate to minimize stray capacitance and noise pickup. In practice both the thermal noise and the shot noise generated by the photodiode are insignificant compared to the preamplifier noise, so the latter sets the sensitivity of the optical receiver. The PIN-FET used in the previous benchmark demonstration is the General Optronics* Model GO PINFET.

While P-I-N photodiodes exhibit unity gain, APDs are internal gain devices. An APD makes use of high electric fields within the photodiode's depletion layer to achieve avalanche operation when photons are incident upon the device. This means that a single photon can cause several electrons to be emitted by the device, in effect generating an internal gain mechanism. The multiplication of photo-generated carriers occurs through impact ionization. The carriers are accelerated by the strong electric field. Upon collision with other atoms, the carriers create more electron-hole pairs. Since more signal current results for a given optical input, it follows that for a comparable preamplifier the receiver sensitivity would increase proportionally compared with a unity-gain detector. In practice, avalanche multiplication also occurs for the dark current (the current flowing within the APD when no optical signal is present), which generates a background shot-noise component. In addition, the random nature of the amplification process also introduces excess noise to the receiver. The amplified dark current and excess noise limits the maximum attainable gain. If too much avalanche gain is employed, the shot noise increases faster than the signal. Likewise, if too little gain is used the preamplifier noise dominates. It follows that an optimum avalanche gain exists for a given operating condition for an APD. Optimum occurs roughly when the noise current from the APD just equals the noise currents from the preamplifier stage. This optimum point must be maintained at all times. An APD requires high-voltage supplies for biasing the device. The high voltage generates the high electric fields necessary for gain. Thus, the gain of the APD is a function of the reverse bias voltage level. The avalanche gain is also highly dependent on temperature, so a temperature-compensated biasing circuit must be designed.

The major advantage of the APD design over the PIN-FET receiver is the presence of the internal gain mechanism. This allows not only higher sensitivity to be achieved but also provides for an improved dynamic range compared to a PIN-FET. The avalanche gain of the system can be lowered when the optical signal is strong by adjusting the APD's bias voltage downward to permit strong signals to be received without overload and distortion occurring in the receiver. The excess noise factor limits practical APD gains to 3 to 10 dB. The net gain in sensitivity obtained from the APD should offset the additional circuit complexity required.

7.4 AMPLIFIER DESIGN

7.4.1 Introduction

The block diagram for the circuit is shown in figure 20. With the increase in performance for the APD receiver invariably comes an increase in complexity. There is the addition of a temperature-compensated voltage regulator. It is designed to maintain constant gain by varying the reverse bias in

* General Optronics, 2 Olson Ave., Edison, NJ 08820, (201) 549-9000

response to changes in temperature. The operation of the temperature-compensated voltage regulator is explained below. After the input optical signal is converted to an electrical signal and amplified by the transimpedance amplifier, there is a DC-blocking capacitor that serves to keep the output impedance of the circuit from affecting the DC-biasing of the transimpedance amplifier. After the DC block, the signal passes through a 50 Ω load so there will be no reflections from the output. Before the signal goes to the decoder, it passes through a linear-phase filter to eliminate high-frequency noise while at the same time retaining the linearity of the signal phase.

The schematic is shown in figure 21. The dotted lines separate the circuit into the various functional blocks. The resistor values of the different summed arms in the temperature-compensated voltage regulator are selected so as to weight their relative effects on temperature compensation on the voltage. The resistors at the collector for the amplifier's first stage set the amount of current biasing for the two cascode transistors. The two resistors that form the voltage divider at the base of the second transistor set the voltage for the collector of the first transistor such that the voltage is roughly in the middle of the supply's voltage range, thus limiting the chance for clipping of the signal. The resistor at the collector of the second transistor sets the current level through the second transistor and sets the voltage at the base of the emitter follower stage to be 1.4V, to limit the DC current that would pass through the feedback resistor. The resistor at the cathode of the APD is used as over-current protection for APD. In earlier designs, a bleeder resistor to ground and a bypass capacitor to the base of the first transistor was put at the anode of the APD to protect the amplifier from possible high voltage caused by a breakdown in the APD, but the APD's stable reverse bias protection has proven that to be unnecessary.

7.4.2 Purpose of Cascode Design

The preamplifier converts low-level current signals from the APD into moderate voltage signals. To accomplish this with a flat frequency response within the receiver passband, given the capacitive impedance of the APD itself, we employ a transimpedance amplifier. The latter is composed of a forward gain block with resistive feedback to provide flat shunt feedback. The high corner frequency response for the forward gain block is obtained by using low stray capacitance and inductance microwave transistors with surface mount packaging. The devices chosen exhibit a very high gain-bandwidth product when operated at the manufacturer's recommended biasing points for L-band application. In this amplifier, however, the transistors are operated in a current-starved biasing mode. This provides a gain-bandwidth product adequate to provide the required open-loop response characteristics and provides a minimum level of shot noise as well. Cascode topology was employed to maximize the gain-bandwidth product of the forward gain block by virtue of canceling the Miller capacitance that would otherwise occur.

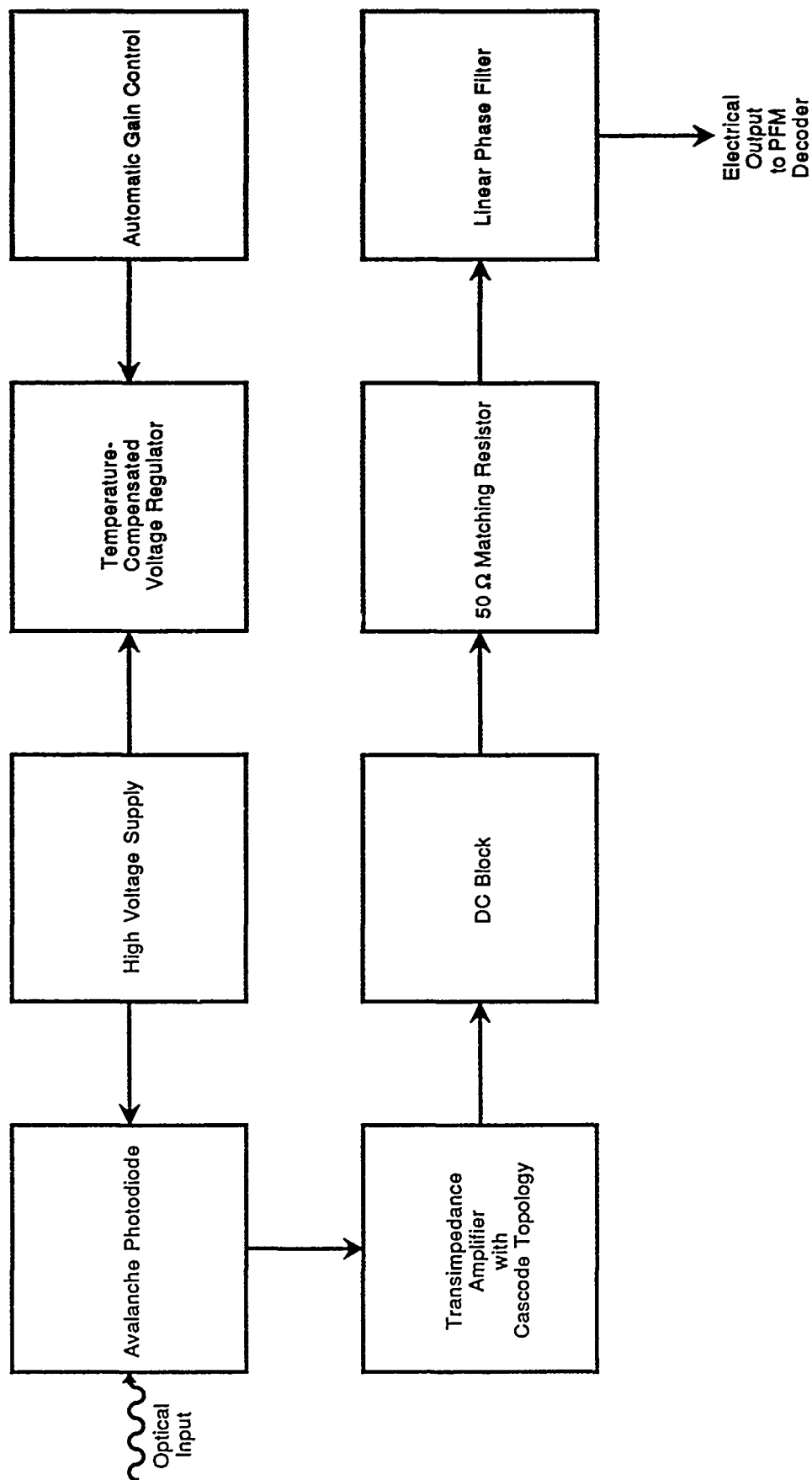


Figure 20. Avalanche photodiode/transimpedance amplifier block diagram.

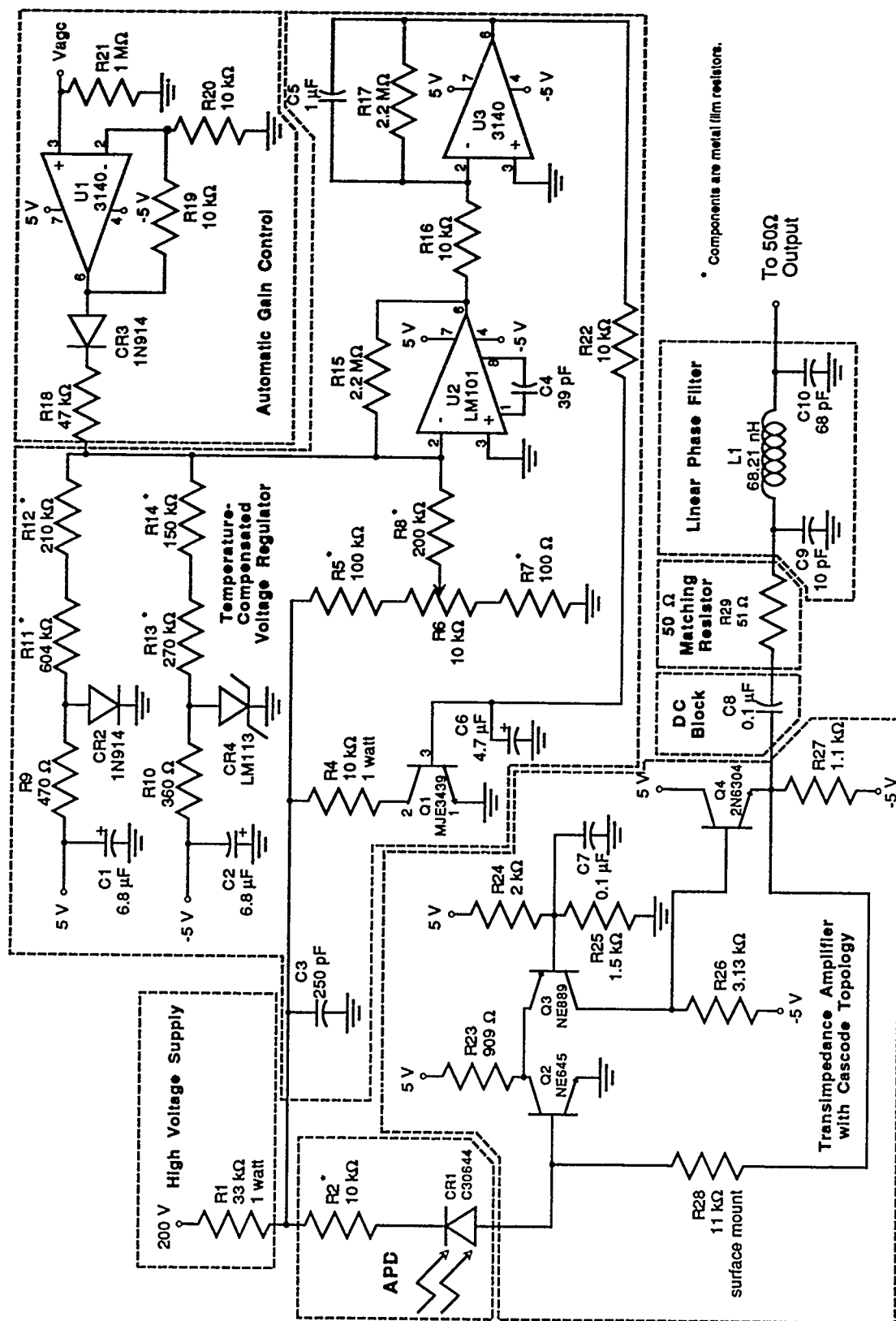


Figure 21. Avalanche photodiode/transimpedance amplifier with temperature-compensated bias and gain controller.

7.4.3 ACNAP Circuit Analysis

To design the amplifier, it was first simulated on a computer using Alternating Current Network Analysis Program (ACNAP) on a Macintosh IIcx. The program represents circuits as networks consisting of four basic elements: resistors, capacitors, inductors, and voltage-dependent current sources. The frequency response of any complex circuit, which can be modeled using these elements, is rapidly calculated by solving the network equations numerically. The ACNAP model for the APD and preamplifier is shown in figure 22. Transistors are modeled using the Hybrid Pi model. Each electrical connection is denoted by a node and a corresponding number. The convention for node numbering is straightforward. The input must be node number 1, and earth ground must be node number 0. These simple building blocks make it easy to model the circuit.

In the circuit, the microwave transistors are represented as subcircuits, using the hybrid- π model for transistors. A spreadsheet was set up to calculate r_π , C_π , and g_m given different collector supply currents and using the gain-bandwidth product and h_{fe} values from each of the transistors' data sheets. The APD is represented with a voltage-dependent current source, with the gain of 1, the voltage source being between the input node 1 and ground. To represent the APD's physical limitations, the APD representation also includes a shunt resistance and a shunt capacitance. A series inductor represents lead inductance. All of the resistors used to bias the microwave transistors include a parallel capacitance of 0.7 pF to take into account the stray capacitance of the carbon resistors that affect their impedance at high frequencies.

The procedure used to optimize the circuit performance is to select a trial bias current for the collector of the first transistor in the cascode forward gain block. The characteristics of this device dominate both the gain-bandwidth product and the shot-noise generation for the entire forward gain block. Increasing the bias current increases both the gain-bandwidth product and the input shot-noise level for the forward gain block. The value of the transimpedance feedback resistor (which in parallel with its stray capacitance forms the return, or feedback, block in the circuit) is then iterated until the required closed loop bandwidth for the preamplifier/APD combination is obtained, say 25 MHz. Smaller resistors, which correspond to increased inverse feedback, result in higher closed loop bandwidth. After the feedback resistor value is determined, its thermal noise-current level is calculated and compared to the shot-noise level calculated from the base current of the first transistor. The noise theorem tells us that the minimum noise figure is achieved when the two levels of noise current (thermal from the feedback resistor and shot from the forward gain block) are equal. In general, the trial value for collector bias does not result in this condition, so the bias is altered and the circuit is re-optimized until the match occurs; the goal is to achieve the required bandwidth with the combination of bias and feedback resistor that results in the lowest noise current, hence the highest optical sensitivity. After this has been achieved, the preamplifier circuit is optimized for noise performance at the given bandwidth. This would be an extremely laborious technique if hand calculations were employed, but the use of a computer makes the technique quite straightforward and quick.

7.4.4 Use of Surface Mount Resistor as Transimpedance Feedback

A surface mount resistor was employed for the feedback resistor because its stray capacitance was lower than 0.25-watt axial-lead types. This permitted a lower noise preamplifier to be designed for a given bandwidth. In fact, the performance of the amplifier is actually limited by the stray capacitance of the feedback resistor and associated wiring. Constructing the device as an integrated circuit would undoubtedly help even more, although this approach was considered to be out of scope for this project.

7.5 TEMPERATURE-COMPENSATED BIAS AND AUTOMATIC GAIN CONTROL

7.5.1 Introduction

APDs have a very effective internal gain mechanism due to controlled avalanche multiplication initiated by the incident photoelectrons. For low avalanche gains, the thermal noise of the preamplifier dominates, while for very high gains the multiplied shot noise from the APD is the dominant noise source. It is apparent that an optimum avalanche gain exists between these extremes for which the noise components are equal. Typical APDs have optimum avalanche gains on the order of 10, and this parameter is supplied with the unit. The gain of the APD is controlled by changing its reverse-bias voltage, with higher bias corresponding to more avalanche gain. However, the bias voltage at which the optimum gain is achieved is susceptible to fluctuations in temperature in practice. In addition, the avalanche gain must be reduced before the signal becomes so strong that the APD starts to saturate either its preamplifier or the PFM decoder. To address these concerns the APD circuit employs both automatic gain control (AGC) circuitry as well as temperature-compensated bias (TCB) voltage regulator circuitry.

Since the relationship between optimum APD bias and ambient temperature is approximately linear over the operating temperature range typically encountered within an environment occupied by humans, the compensation voltage is easily derived by monitoring the v_{be} drop on an ordinary silicon diode in close physical proximity to the APD and scaling its magnitude accordingly.

7.5.2 Circuit Function

The high voltage applied to the APD is reduced by a precision voltage divider to voltage levels that can be processed by operational amplifiers. This voltage is compared with a precision, temperature-compensated reference voltage by means of an integrating analog error amplifier. If the APD bias voltage attempts to increase above the preset level, the error amplifier supplies additional base current to a high-voltage transistor in parallel with the APD. The parallel transistor acts as a shunt regulator, reducing the APD bias accordingly. The entire circuit forms a precise, high-voltage regulator with inverse feedback.

7.5.3 Automatic Gain Control Interface

The AGC control signal is generated by the PFM decoder circuit. For weak signals the AGC voltage is less than 0.6 volts, but as the optical signal becomes intense enough to cause decoder circuit overload the AGC voltage exceeds 0.6 volts. When this occurs, a silicon diode within the APD controller begins to conduct, and the reference voltage to the regulator is automatically reduced in a proportional manner, preventing overload from occurring. This mechanism is effective until the APD bias is reduced below the point where full depletion of the PN junction of the APD occurs. Since the optimum APD gain is on the order of 10 and the APD performance begins to degrade below a gain of about 1 or 2, an increase in the receiver optical dynamic range of 7 to 10 dB results from the incorporation of the AGC loop.

7.5.4 Temperature-Compensated Voltage Regulator

The precision reference voltage is a composite signal that consists of three components: constant voltage (derived from a compensated voltage reference), a temperature-variable voltage (derived from

the v_{be} drop of a silicon diode located in close physical proximity to the APD), and the AGC voltage (only if it exceeds 0.6 volts). The proportion of *constant to variable* reference voltage is set (by the ratio of two fixed resistors) according to the bias versus temperature coefficient provided by the APD manufacturer (in $mV/^\circ C$). Once adjusted, the bias varies in such a way as to keep the gain of the APD relatively constant over a moderately wide range of temperatures.

7.5.5 Adjustment of Temperature Control

The APD's manufacturer supplies information on the bias voltage as a function of temperature that is optimum for that device to hold it at the optimum gain in $mV/^\circ C$. Once the high voltage is adjusted for the optimal voltage, the circuit is tested in a temperature chamber, letting the temperature fluctuate across a reasonable span ($2^\circ C$ to $52^\circ C$). If the voltage change required for constant gain needs to be increased, the gain of the variable arm of the precision reference is increased, and vice versa. As the proportion of the variable reference is changed, the resistance of the constant reference arm must also be changed so the sum remains constant. These two resistance values can be adjusted until the APD bias closely approximates the voltage recommended by the manufacturer for constant gain over a wide range of ambient temperatures.

7.6 FILTER DESIGN

Since the receiver detects pulses, the system must approach a linear phase response to prevent ringing and corresponding intersymbol interference. A linear phase lowpass filter follows the preamplifier to remove out-of-band noise. The bandwidth of the filter is chosen so that when cascaded with the preamplifier a net system bandwidth, measured at the -3 dB point, of 32 MHz results. A standard reference handbook was consulted to determine the component values for the linear phase filter (Hansell, 1969).

A simple spreadsheet routine was set up to calculate the inductor and capacitor values. Standard value capacitors were used, so to tune the filter to the correct frequency a variable inductor was employed that used an adjustable ferrite slug. The inductor was adjusted so the most favorable frequency and phase response occurred. Through the use of a network analyzer, the filter was easily adjusted to yield the desired bandwidth and phase linearity.

7.7 EXPERIMENTAL RESULTS

This section details the results of measurements made on the APD receiver. Included are measurements of receiver bandwidth and sensitivity, preamplifier noise, performance of the temperature-compensated bias control circuit, and receiver dynamic range using the PFM AGC.

7.7.1 APD Receiver Bandwidth

The bandwidth of the APD receiver was measured. Two techniques are used. The receiver risetime is measured and the 3-dB bandwidth is derived from the risetime using the relation

$$BW_{3-dB} = 0.35 / t_{RX} . \quad (19)$$

The measured APD receiver risetime was 11.3 ns for a resultant bandwidth of 31 MHz. This compares favorably to the goal of 32 MHz. The APD performance is compared to the original PIN-FET by placing a low-pass filter at the output of the PIN-FET receiver with roll-off set so each receiver has equivalent bandwidths. A 40-MHz filter follows the 50-MHz PIN-FET to give a net 31.2-MHz

bandwidth. Based on the results of the wider pulse width for the PFM transmission, the present 31-MHz APD receiver bandwidth is adequate to process the 16-ns pulse.

Figure 23 plots the frequency response of the APD preamplifier as predicted by the ACNAP model. Shown also is the measured bandwidth of the receiver. The bandwidth was found by a spectrum analyzer. It is seen that the model closely predicts the circuit performance. The model predicts a bandwidth of 32 MHz. The measured bandwidth was 31.2 MHz.

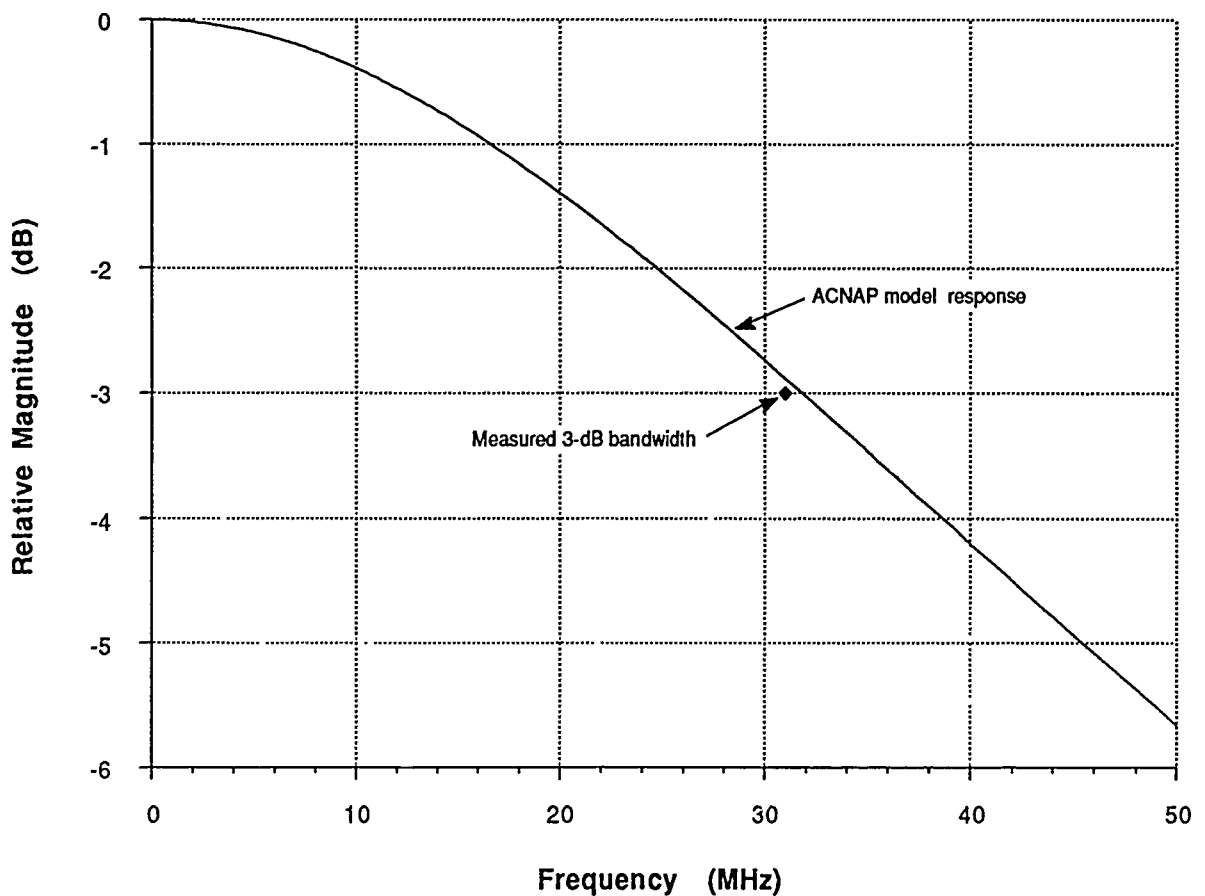


Figure 23. Frequency response of APD receiver: ACNAP model and measured -3 dB point.

7.7.2 APD Receiver Sensitivity

Table 4 lists the *measured* performance data for the InGaAs APD used in the system.

Table 4. Measured performance data for RCA InGaAs APD.

Manufacturer: RCA Inc., Electro-Optics		
Model: C30645EQC-02		
Bias voltage ($M \sim 10$)	70.7	Volts
Responsivity ($M \sim 10$, 1300 nm)	8.0	A/W
Total dark current	144	nA
Noise-current density	0.95	pA/ $\sqrt{\text{Hz}}$
Bulk dark current ($M = 1$)	5	nA
k_{eff}	0.45	
Frequency (3 dB)	>1000	MHz
Fiber pigtail	50/125	μm

These values are incorporated into the theoretical analysis to predict the performance of the APD/preamplifier using the APD receiver built at NOSC and the actual APD data. The bandwidth is 32 MHz and the C/N = 16 dB. The APD preamplifier noise was measured. The noise attributed to shot noise from the transistor bias currents was measured at 1.26 pA/CHz, and the thermal noise from the feedback resistor was 1.23 pA/ $\sqrt{\text{Hz}}$. The total preamplifier noise is the root-sum-square of these values or 1.76 pA/ $\sqrt{\text{Hz}}$. This value is inserted into the preamplifier noise portion of the C/N equation, equation 18. The APD noise is computed based on the values listed above. The measured noise current density of the APD was 0.95 pA/ $\sqrt{\text{Hz}}$. The theoretical optimum APD receiver sensitivity was found to be -48.6 dBm, peak. This is roughly 3 dB better than the 50-MHz PIN-FET. An improvement of 2 dB is attributed to the reduction in bandwidth.

The APD sensitivity was indirectly measured. A 16-ns pulse was transmitted from the PFM encoder. An optical attenuator was used to lower the power level incident on the APD until threshold C/N of 16 dB was reached. The attenuator loss was noted. Next the same operation was performed on the original 50-MHz PIN-FET using a transmitted pulse width of 12 ns. The attenuator loss was 6 dB less for the PIN-FET. This means that the 32-MHz APD sensitivity is 6 dB better than the original 50-MHz PIN-FET, or approximately -51.75 dBm. Figure 24 compares measured performance against predicted performance for the APD receiver. The measured APD sensitivity is placed at the optimum predicted gain; however, the manufacturer specifies a gain of 10 for its measurements. Also shown is the 50-MHz PIN-FET sensitivity. The net gain of 6 dB is divided into two components: 2 dB is from the reduction in bandwidth and 4 dB is from the APD gain.

The measured APD sensitivity of -51.75 dBm does not compare closely to the theoretical prediction of -48.6 dBm. Several sources of error and uncertainty are noted. The uncertainty of the measured APD sensitivity is based on the precision of the PIN-FET sensitivity (± 0.5 dB), the repeatability of the insertion loss at the APD and PIN-FET fiber pigtails (± 0.35 dB), the repeatability of the attenuator (± 0.5 dB), and the ability to find the C/N = 16 dB threshold point (± 0.25 dB). Together this gives a measured uncertainty of ± 1.6 dB. The theoretical APD sensitivity, as derived from the equation 18 is full of variables that present uncertainties. In particular, the uncertainties of responsivity ($\pm 10\%$), total dark current ($\pm 50\%$), and preamplifier noise current ($\pm 25\%$) values cause a total theoretical sensitivity uncertainty of roughly ± 1.1 dB. The error bars for the measured and theoretical sensitivities are included on the plot in figure 24.

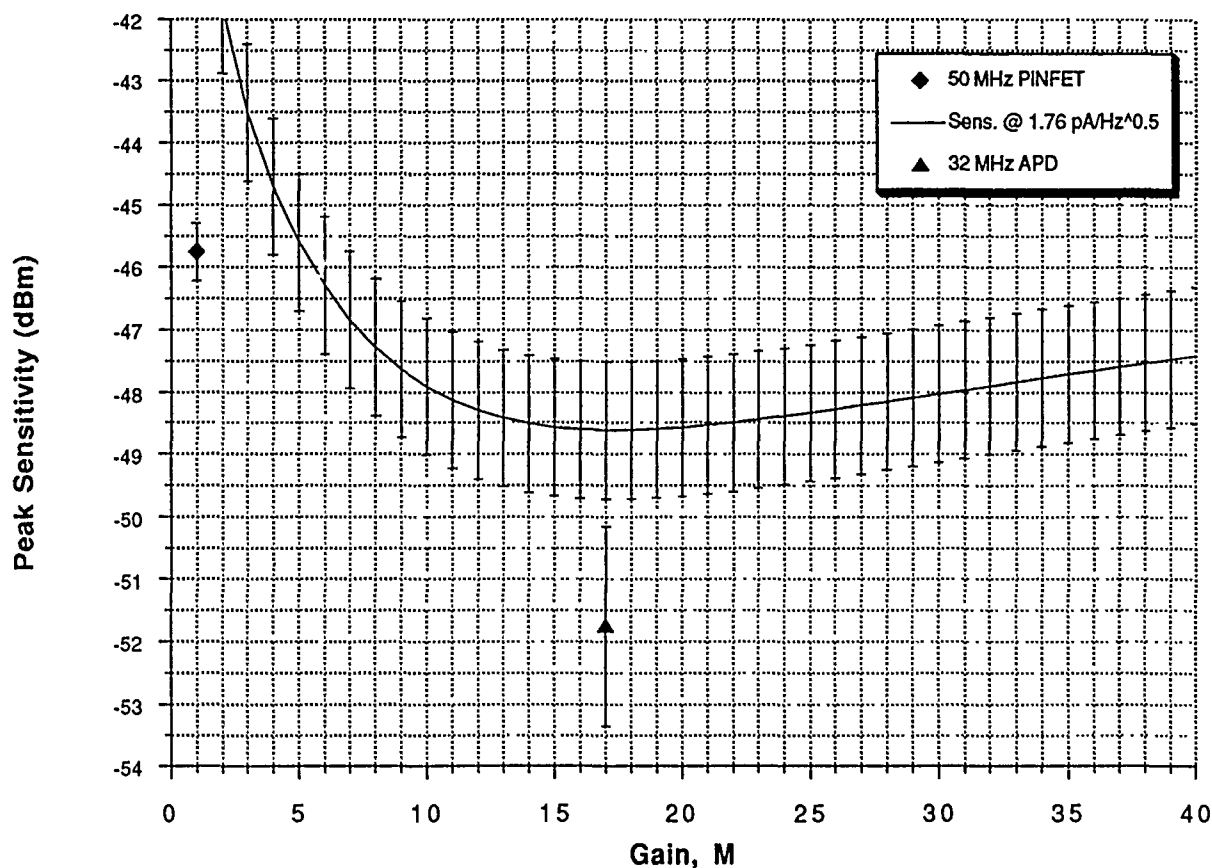


Figure 24. Theoretical and measured sensitivities for the PIN-FET and APD receivers.

7.7.3 Testing of Temperature-Compensated Bias Control Circuit

The temperature-compensated bias control circuit was tested. The temperature testing was done in a high-precision temperature chamber. The temperature was allowed to settle for approximately 45 minutes, and the voltage across the APD was measured with respect to its temperature. The slope of voltage versus temperature was then calculated. The temperature was changed in 10°C increments to test for linearity.

When the voltage versus temperature slope is calculated, the resistor values for the thermistor arm and the reference arm are adjusted. If there needs to be a greater change in voltage with respect to temperature, more current must come from the thermistor arm. The opposite is true when a smaller change in voltage with respect to temperature is required. The APD manufacturer recommends a voltage change for constant gain of 0.18 V/°C. It is necessary to get as close to that coefficient as possible.

The final results are shown in table 5.

Table 5. Results of temperature-compensated bias circuit testing.

Temperature(°C)	Voltage (V)	Slope(V/°C)
2	75.51	—
12	77.84	0.233
22	80.24	0.240
32	82.66	0.242
42	85.07	0.241
52	87.53	0.246

7.7.4 Receiver Dynamic Range Using the PFM AGC

Dynamic range measurements are made when the AGC output from the PFM decoder is connected to the AGC input of the APD receiver. The results are compared to the dynamic range of the PIN-FET where no AGC is employed. The PIN-FET receiver delivers an average dynamic range of 32 dB, measured as the margin between the low input power threshold point of the PFM circuitry and where the PIN-FET saturates from high input power. This number compares favorably to the 30-dB value given by the manufacturer. When the AGC circuitry is used for the APD receiver, a dynamic range of 38 dB is recorded. This increase is divided into the 6 dB achieved from the internal gain and reduced bandwidth of the APD, and an additional 2 dB more range is seen at the high input power edge.

8.0 EMERGING TECHNOLOGIES

This section discusses two emerging technologies that will be integrated into the demonstration project in the near future. They are the fiber amplifier and the DFB laser transmitter.

8.1 FIBER AMPLIFIERS

One technology rapidly advancing is the fiber amplifier (Becker, 1990, and Desurvire, 1990). A coil of fiber, typically 10 to 100 meters long, is lightly doped with trivalent rare-earth ions such as erbium. The fiber coil is then excited with a laser-diode pump source using a fused biconical-taper WDM to couple the pump power into the coil. The pump power raises the rare-earth ions in the fiber coil to an excited metastable state of population inversion. Under this condition, according to quantum electronics, a signal passing through the coil with a wavelength equivalent to the transition between excited and ground states experiences a net gain due to stimulated emission. For erbium, using a 1480-nm pump, this gain occurs in a spectral band between 1525 and 1565 nm. Gains of 10 to 30 dB have been realized.

Fiber amplifiers have many outstanding features, a few of which are listed here. The fiber geometry offers unique advantages. The pump and signal powers are confined to a very small core area over an extended interaction length. This provides for efficient pump absorption over long lengths (Mears, Reekie, Jauncey, and Payne, 1987). The fiber gain is polarization insensitive. The fiber is easily interfaced to the transmission line fiber. Fusion splices give low-loss, low-reflection coupling. Fiber amplifiers are potentially more reliable and smaller than their opto-electronic counterparts. Unlike opto-electronic repeaters, the fiber amplifiers are essentially bit rate transparent. Experiments have shown a limit in the Tbit/s range (Grasso, Cheung, and Righetti, 1989). The future will see rapid advances in gain performance and packaging of these devices as they become widely adopted for an assortment of long-distance, multiaccess distribution network, and sensor applications.

Figure 25 is an optical diagram of a proposed fiber preamplifier experiment. It will be applied to the demonstration project in FY 91. As shown, the fiber amplifier is inserted in the optical line at the receive end of the 1550-nm channel, prior to the receiver. Also shown in the figure are the anticipated optical spectra at three places in the preamplifier stage. At Point A, the spectrum is solely the attenuated signal spectrum from the Fabry-Perot laser-diode transmitter, centered at 1550 nm. The local 1300-nm laser spectrum is isolated from this point by the WDM. At Point B, the output of the fiber amplifier, the spectrum now includes three main features. The signal spectrum is now amplified by the fiber amplifier. The laser pump spectrum is also present. The coupled pump power into the amplifier is quite high, 50 mW, however the pump is configured in a counter-propagating pump mode, reducing the backscattered output level significantly. Finally there is the amplified spontaneous emission (ASE) from the pumped erbium. This is relatively broad, continuous, and identical to the shape of the gain spectrum. The tunable optical bandpass filter (OBPF) is tuned to the signal center wavelength. The bandpass width is set slightly larger than the emission spectral width of the signal. The OBPF rejects the erbium-doped fiber amplifier (EDFA) pump spectrum and the out-of-band ASE spectrum. Of course, the in-band ASE is passed through the filter along with the signal. This in-band noise from the ASE reduces the ultimate gain advantage the preamplifier can provide by reducing the optical-carrier-to-optical-noise ratio. Both PIN-FET and APD receivers will be evaluated with the optical preamplifier.

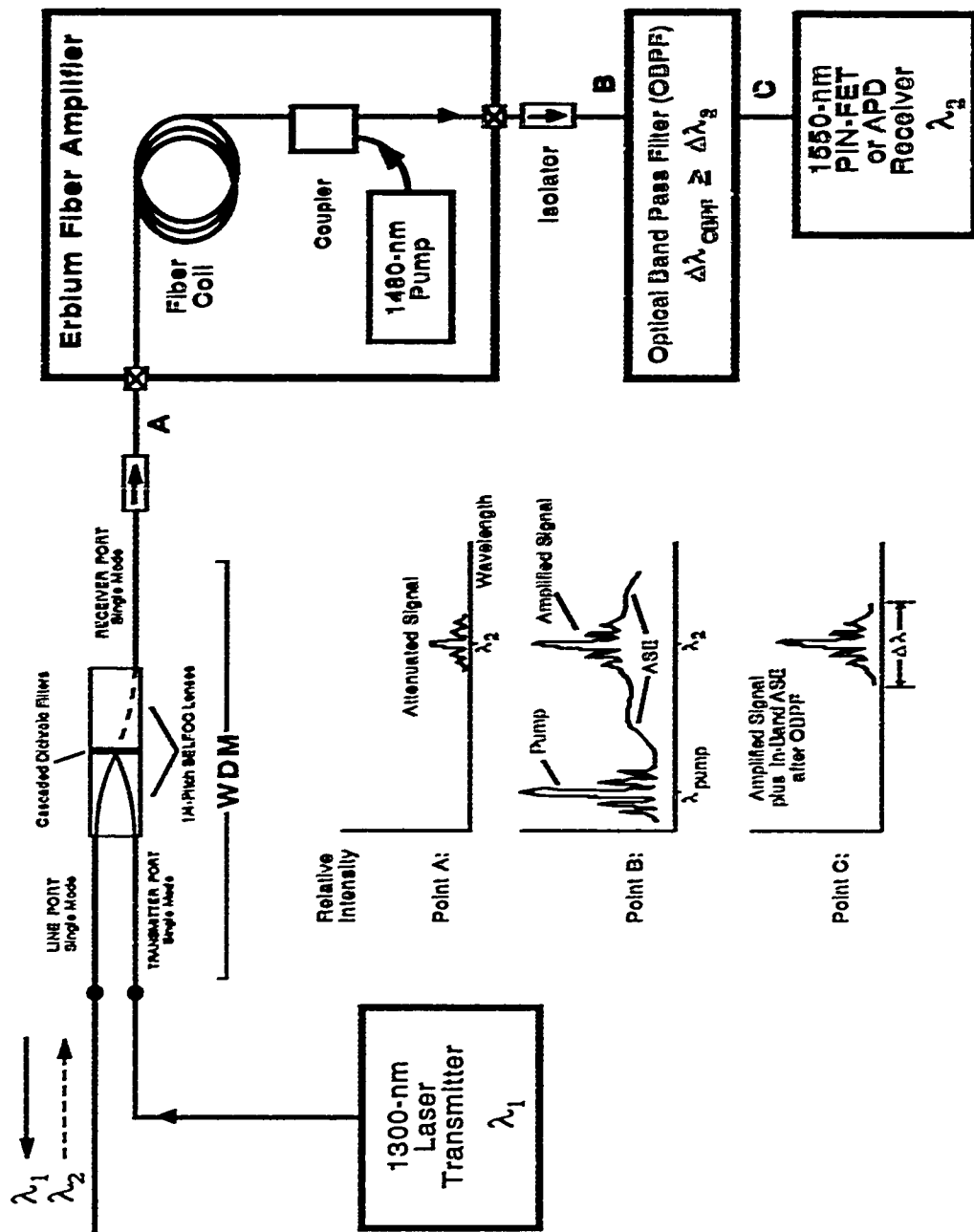


Figure 25. Optical diagram of an erbium-doped fiber preamplifier.

Measurements must be taken to characterize the spectra and spectral response of the components. A net gain measurement will establish the effectiveness of the amplifier in the presence of optical noise. Future attempts will be directed at employing narrow-line DFB lasers as signal transmitters and using high-finesse, tunable Fabry-Perot etalons in addition to interference filters to reject as much unwanted ASE as possible. Results of these tests and the performance of the EDFA as a preamplifier in the 1550-nm channel will be given in a follow-up report. It is hoped to obtain 10 to 15 dB of gain for the 1550-nm channel using a fiber preamplifier.

8.2 DISTRIBUTED-FEEDBACK LASER TRANSMITTERS

The laser transmitters employed in the present system are Fabry-Perot type. As such they exhibit multi-longitudinal-mode spectral characteristics. Typical spectral widths are 2 to 4 nm, or about 3 to 5 longitudinal modes. As was shown in the dispersion-limited range section of this report, the spectral width of a Fabry-Perot laser limits transmission range to roughly 200 to 300 km. Distributed feedback or DFB lasers have significantly narrower spectral emissions. A sinusoidal grating is etched on top of the active layer of the laser cavity and, through Bragg diffraction, causes the DFB laser to amplify and emit a single longitudinal mode. When the DFB is operated continuous wave, this mode has a typical FWHM linewidth of only 50 MHz (at 1550 nm, 125 GHz = 1 nm). This reduced spectral width virtually eliminates the dispersion-limited range constraint.

Another advantage of the narrow-linewidth DFB laser is for use with the EDFA. Signal transmission with a DFB laser allows an extremely narrow bandpass filter to be used at the output of the fiber preamplifier. A relatively broad-band interference filter is followed by a high-finesse Fabry-Perot etalon filter. The etalon filter rejects over 100 times as much ASE noise from the fiber amplifier as the interference filter does, with a corresponding reduction in optically generated noise at the detector. The interference filter is used to reject all but one of the Fabry-Perot etalon resonance orders. The use of the DFB laser and etalon filter with the erbium-doped fiber preamplifier will greatly enhance the receiver sensitivity.

DFB lasers housed in transmitter packages have recently become available. These are similar to the Fabry-Perot transmitters. They contain bias and temperature-compensated control circuits to maintain constant output power and center emission wavelength. It is planned to incorporate a 1550-nm DFB laser transmitter and a feedback-controlled, tunable Fabry-Perot filter into the system during early FY 92.

9.0 CONCLUSIONS

This report discussed improvements made to the long-distance, repeaterless, duplex fiber-optic demonstration system. Improvements in laser output power and receiver sensitivity were realized. These upgrades resulted in extended standoff range performance compared to results noted in the original 104-km report. Ultimate distances of 186 km are now possible under conditions of optimal fiber attenuation. Nominal standoff range is 153 km for fiber attenuation of 0.45 dB/km at 1300 nm.

Plans for FY 91 and early FY 92 call for installing an erbium-doped fiber amplifier in line as a preamplifier to the 1550-nm receiver and using a DFB laser transmitter at 1550 nm. This approach is useful since future applications may well employ pulse code modulation (PCM) (which is less efficient than PFM, in general) and will require higher bandwidth. Higher bandwidth would reduce the loss margin available at the 1550-nm wavelength. The extra operating margin gained from a DFB/EDFA combination, therefore, could become very important at a later time.

The future for fiber amplifiers operating at 1300 nm is uncertain. The present emphasis is at 1550 nm since this is the window of lowest attenuation and highest bandwidth for silica-based dispersion-shifted optical fiber. However, fiber amplifiers using a fluoride glass host and doped with neodymium instead of erbium have been made (Miyajima, Sugawa, and Komukai, 1990). These amplifiers exhibit small-signal gains of 5 to 10 dB in the 1300- to 1360-nm range, with optimum gain at 1330 nm. Many technical issues must be addressed, especially concerning excited state absorption around 1300 nm (Dakss and Miniscalco, 1990). This condition can cause loss instead of gain, depending on the composition of the glass host. Currently the amplifiers compare poorly to erbium-doped amplifiers for use as preamplifiers, however they show promise as booster amplifiers, placed just after the 1300-nm laser transmitter. Topologically, this may prove to be beneficial. It would allow both 1550-nm fiber preamplifier and 1300-nm fiber booster or postamplifier to be physically located together.

At present, 1300-nm fiber amplifiers are not available off the shelf. The lack of a 1300-nm fiber amplifier impacts the standoff range for the demonstration system. Originally the range was limited by the 1300-nm channel. Then the low-noise integrating receiver and high-power laser transmitter were installed in the 1300-nm channel and the limit shifted to the 1550-nm channel. Finally, with the implementation of the APD receiver and the wider pulse width PFM circuitry for the 1550-nm channel, the limit has shifted back to the 1300-nm channel.

A new multiplexing approach is currently being considered that would solve the 1300-nm limitation problem. The technique calls for separating the two duplex channels by only 25 nm instead of the present separation of 250 nm. One channel would operate at 1535 nm and the other at 1560 nm. This approach allows both channels to take advantage of the low fiber attenuation and the availability of erbium-doped fiber preamplifiers. Recent advances in DFB transmitters and very narrow bandpass filters make it possible to place adjacent channels very close to each other. The level of crosstalk between the two channels establishes the ultimate limitation of this approach. Current filter technology provides for isolations of 40 to 70 dB depending on the blocking material used. Another filtering technique would use cascaded, fused-biconical-taper (FBT) WDMs to separate the two channels. As noted in this report, isolations of 80 to 100 dB are needed due to the duplex configuration, that is the need to isolate a powerful local signal from a weak, remotely transmitted signal. Many parametric tradeoffs must be considered before implementation of this approach is practical. Issues such as increased insertion loss versus isolation, transmitter and filter stability, and increased filter complexity must be addressed.

For the near future, it appears the link will remain limited at 1300 nm, since the EDFA will only serve to further extend the 1500-nm channel range. Near-term approaches for solving the 1300-nm channel limitation will be investigated and implemented as the technology becomes available. These approaches include future upgrades of the 1300-nm laser transmitter, the possible addition of an APD to the low-bit-rate receiver, and installation of a neodymium-doped fiber power amplifier. In parallel to this, the new multiplexing scheme will be analyzed. Implementation of these upgrades will ultimately extend the system standoff range.

10.0 REFERENCES

- Becker, P. C. 1990. "Erbium-Doped Fiber Makes Promising Amplifiers," *Laser Focus World*, pp. 197-203, October.
- Brininstool, M. 1987. "104-km Unrepeated Bidirectional Fiber-Optic Demonstration Link", NOSC TR 1185. (May) Naval Ocean Systems Center, San Diego, CA.
- Cowen, S. J. 1979. "Fiber-Optic Transmission System Employing Pulse Frequency Modulation," *IEEE of Proceedings of Oceans*, pp. 253-259, September.
- Dakss, M. L., and W. J. Miniscalco. 1990. "Limits of Performance of a Nd^{3+} -Doped Fiber Amplifier at 1.3 μm ," *Proceedings of Optical Amplifiers Topical Meeting*, Paper TuD3, pp. 175-178, 6-8 August. Monterey, CA.
- Desurvire, E. 1990. "Erbium-Doped Fiber Amplifiers for Optical Fiber Communications," *Proceedings of Optical Amplifiers Topical Meeting*, Paper MB1, pp 8-11, 6-8 August. Monterey, CA.
- Grasso, G., N. K. Cheung, and A. Righetti. 1989. "An 11 Gbit/sec 260 km Transmission Experiment Using a Directly Modulated DFB Laser with Two ER-Doped Amplifiers and Clock Recovery," *ECOC (Gothenburg) Postdeadline Session Paper PDA 10*.
- Hansell, G. E. 1969. *Filter Design and Evaluation*, Van Nostrand Reinhold Co., © pp. 1-4.
- Mears, R. J., L. Reekie, I. M. Jauncey, and D. N. Payne. 1987. "Low-Noise Erbium-Doped Fibre Amplifier Operating at 1.54 μm ," *Electronic Letters*, vol. 23, no.19, pp 1026-28.
- Miyajima, Y., T. Sugawa, and T. Komukai. 1990. "1.3/1.55 μm Band Simultaneous Amplifier Comprising Nd^{3+} -Doped and Er^{3+} -Doped Fluoride Fibers", *Proceedings of Optical Amplifiers Topical Meeting*, Paper TuD2, pp.171-174, 6-8 August 1990. Monterey, CA.
- Morris, D. 1983. *Pulse Code Formats for Fiber-Optical Data Communication*, vol. 5, Marcel-Dekker, New York, pp. 27-138.
- Sander, L. 1982a. "Pulse Codes in Serial Data Communications," *Computer Design*, pp 203-210, January.
- Sander, L. 1982b. "Improve Datacomm Links by Using Manchester Code," *EDN*, pp 155-162, February.
- Yariv, A. 1976. *Introduction to Optical Electronics*, (Second Edition), Holt, Rinehart, Winston, New York, p. 295.

REPORT DOCUMENTATION PAGE

Form Approved
OMB No. 0704-0188

Public reporting burden for this collection of information is estimated to average 1 hour per response, including the time for reviewing instructions, searching existing data sources, gathering and maintaining the data needed, and completing and reviewing the collection of information. Send comments regarding this burden estimate or any other aspect of this collection of information, including suggestions for reducing this burden, to Washington Headquarters Services, Directorate for Information Operations and Reports, 1215 Jefferson Davis Highway, Suite 1204, Arlington, VA 22202-4302, and to the Office of Management and Budget, Paperwork Reduction Project (0704-0188), Washington, DC 20503

1. AGENCY USE ONLY (Leave blank)		2. REPORT DATE February 1991		3. REPORT TYPE AND DATES COVERED Interim	
4. TITLE AND SUBTITLE LONG-DISTANCE REPEATERLESS DUPLEX FIBER-OPTIC DEMONSTRATION SYSTEM				5. FUNDING NUMBERS PE: 3000N PROJ: CG92 SUBPROJ: 946-CG92 ACC: DN188 527	
6. AUTHOR(S) M. R. Brininstool, S. J. Cowen, W. H. Marn, and M. C. Scallan					
7. PERFORMING ORGANIZATION NAME(S) AND ADDRESS(ES) Naval Ocean Systems Center San Diego, CA 92152-5000				8. PERFORMING ORGANIZATION REPORT NUMBER NOSC TR 1411	
9. SPONSORING/MONITORING AGENCY NAME(S) AND ADDRESS(ES) Chief of Naval Operations Washington, DC 20350				10. SPONSORING/MONITORING AGENCY REPORT NUMBER	
11. SUPPLEMENTARY NOTES					
12a. DISTRIBUTION/AVAILABILITY STATEMENT Approved for public release; distribution is unlimited.				12b. DISTRIBUTION CODE	
13. ABSTRACT (Maximum 200 words) This report updates Naval Ocean Systems Center TR 1185, "104-km Unrepeated Bidirectional Fiber-Optic Demonstration Link," May 1987. Provided are discussions on improvements made to the original demonstration system. These include enhanced receiver sensitivities, increased laser-transmitter optical power outputs, refined operation of the PFM and Manchester encoding subsystems, and reduced splice losses. Also discussed is the emerging technology of fiber amplifiers that promise to significantly extend the repeaterless distance beyond the present range.					
14. SUBJECT TERMS fiber optics pulse-frequency modulation laser diodes wavelength-division multiplexers photodiodes Manchester encoding fiber amplifiers avalanche photodiodes				15. NUMBER OF PAGES 64 16. PRICE CODE	
17. SECURITY CLASSIFICATION OF REPORT UNCLASSIFIED	18. SECURITY CLASSIFICATION OF THIS PAGE UNCLASSIFIED	19. SECURITY CLASSIFICATION OF ABSTRACT UNCLASSIFIED	20. LIMITATION OF ABSTRACT SAME AS REPORT		

UNCLASSIFIED

21a. NAME OF RESPONSIBLE INDIVIDUAL M. R. Brininstool	21b. TELEPHONE (include Area Code) (619) 553-1952	21c. OFFICE SYMBOL Code 946

INITIAL DISTRIBUTION

Code 0012	Patent Counsel	(1)
Code 0141	A. Grodon	(1)
Code 0142	K. Campbell	(1)
Code 0144	R. November	(1)
Code 02	H. R. Talkington	(1)
Code 17	R. T. Shearer	(1)
Code 1742	J. Boyle	(1)
Code 534H	N. Kamikawa	(1)
Code 534H	A. Nakagawa	(1)
Code 55	H. Rast	(1)
Code 553	G. Garcia	(1)
Code 553	D. Albares	(1)
Code 555	S. Pappert	(1)
Code 555	M. McLandrich	(1)
Code 702	B. Hearn	(1)
Code 7103	B. Smith	(1)
Code 714	J. Ehlers	(1)
Code 714	K. Rogers	(1)
Code 732	D. Morin	(1)
Code 761	D. Gookin	(1)
Code 761	M. Berry	(1)
Code 765	D. Williams	(1)
Code 82	B. Kochanski	(1)
Code 821	B. Gallanberger	(1)
Code 821	D. Butts	(1)
Code 90	I. Lemaire	(1)
Code 92	G. Kosmos	(1)
Code 934	A. Flores	(1)
Code 934	C. Hansen	(1)
Code 94	N. Estabrook	(1)
Code 941	M. Kono	(1)
Code 941	R. Marrone	(1)
Code 942	B. Bixler	(1)
Code 942	W. Stevenson	(1)
Code 942	S. Briest	(1)
Code 942	B. Watts	(1)
Code 942	J. Zuniga	(1)
Code 943	D. Bryan	(1)
Code 943	A. Waltz	(1)
Code 943	P. Heckman	(1)
Code 944	B. Wernli	(1)
Code 946	S. Cowen	(30)
Code 946	M. Brininstool	(50)
Code 946	B. Marn	(30)
Code 946	M. Scallon	(30)

Defense Technical Information Center Alexandria, VA 22304-6145	(4)
Defense Advanced Research Projects Agency Arlington, VA 22217-5000	(10)
Office of the Assistant Secretary of the Navy Washington, DC 20360-5000	
Naval Air Systems Command Washington, DC 20361-0001	(2)
Space & Naval Warfare Systems Command Washington, DC 20363-5100	
Naval Research Laboratory Washington, DC 20375-5000	(7)
Naval Underwater Systems Center New London Laboratory New London, CT 06320	(2)
Naval Underwater Systems Center Newport, RI 02841-5047	(2)
Naval Electronic Systems Engineering Center Charleston, SC 29406	
Naval Undersea Warfare Engineering Station Keyport, WA 98345	(2)
Naval Surface Warfare Center Silver Spring, MD 20910	
Office of Naval Intelligence Washington, DC 20350-2000	(10)
Naval Civil Engineering Laboratory Port Hueneme, CA 93043-5003	
Naval Coastal Systems Center Panama City, FL 32407	(7)
Naval Weapons Center China Lake, CA 93555-6001	(6)
PEO for Submarine & Combat Weapons Washington, DC 20360	(3)
Office of Naval Technology Arlington, VA 22217-5000	
Office of Naval Research Arlington, VA 22217-5000	(5)

Naval Postgraduate School
Monterey, CA 93943 (5)

Marshall Spaceflight Center
Space Sciences Laboratory
Huntsville, AL 35812

MICOM
Huntsville, AL 35812

U.S. Air Force Rome Development Center
Hanscom Air Force Base
Bedford, MA 01731 (2)

Arizona State University
Tempe, AZ 85287-7506

Johns Hopkins University
Applied Physics Laboratory
Laurel, MD 20707 (2)

Pennsylvania State University
Applied Research Laboratory
State College, PA 16801 (11)

University of Hawaii
Hawaii Institute of Geophysics
Honolulu, HI 96822 (2)

Applied Remote Technology (ART)
San Diego, CA 92121

AT&T Bell Laboratories
Whippany, NJ 07981 (2)

AT&T Bell Laboratories
Norcross, GA 30071 (2)

AT&T Network Systems
Atlanta, GA 30328

AT&T Technologies, Inc.
Greensboro, NC 27420 (2)

AT&T Technologies, Inc.
San Diego, CA 92121

ATT Murray Hill
Murray Hill, NJ 07974

Corning Glass Works
Corning, NY 14831 (2)

Draper Laboratories
Cambridge, MA 02139

Lockheed Marine Systems
Sunnyvale, CA 94088

SEI
San Diego, CA 92108

TRW
Redondo Beach, CA 92078

Westinghouse
Oceanic Division
Annapolis, MD 21404 (10)